International Journal of Heat and Mass Transfer 194 (2022) 123101

Contents lists available at ScienceDirect

International Journal of Heat and Mass Transfer

journal homepage: www.elsevier.com/locate/hmt

Flow boiling in copper and aluminium microchannels

Ali H. Al-Zaidi [a], Mohamed M. Mahmoud [b], Tassos G. Karayiannis [c,*]

[a] University of Misan, Al-Amarah, 62001, Iraq
[b] Faculty of Engineering, Zagazig University, Zagazig, 44519, Egypt
[c] Department of Mechanical and Aerospace Engineering, Brunel University London, Uxbridge, UB8 3PH, UK

ARTICLE INFO

Article history:
Received 29 November 2021
Revised 21 March 2022
Accepted 1 June 2022
Available online 13 June 2022

Keywords:
Microchannel heat sinks
Electronics cooling
Flow boiling
Surface material
Flow patterns
Heat transfer
Pressure drop
aluminium heat sink

ABSTRACT

The substrate material and active side characteristics can affect the bubble ebullition cycle and consequently the heat transfer rate and pressure drop in microchannel evaporators. This paper presents an experimental study on flow boiling patterns, heat transfer rates and pressure drop in multi-microchannels evaporators made of copper and aluminium. HFE-7100 was used as the test fluid at atmospheric pressure, 5 K inlet sub-cooling, mass flux of 50-250 kg/m^{2}s and wall heat flux up to 174 kW/m^2. All heat sinks were made with channel width 0.46 mm, channel height 0.46 mm, giving a 0.46 mm channel hydraulic diameter. The heat sink base area was 25 mm in length and 20 mm in width. The experimental results showed that similar flow patterns were visualised for copper and aluminium namely bubbly, slug, churn and annular flow. The heat transfer coefficient in the aluminium heat sink was 12% (average value) higher than that found in the copper heat sink. The measured pressure drop in the aluminium heat sink was 28% (average value) higher compared to the copper heat sink. However, the additional pumping power required to move the fluid through the heat exchanger is small for this factor to be significant. The SEM images of the surface revealed that the number of cavities (possible nucleation sites) was higher in the aluminium surface with clear-cutting marks compared to the copper surface. This may explain the different pressure drop and heat transfer behaviour. The results of the present study indicate that aluminium heat sinks can offer comparable thermal performance to that of copper heat sinks and can also be recommended for cooling high heat flux systems.

1. Introduction

The thermal management of electronic equipment that generate a large amount of heat and have a small surface area is still very challenging. Examples of these equipment include electronic components in computers, Laser Diode Bars, Metal Oxide Semiconductor Field-effect Transistors, Insulated-Gate Bipolar Transistor Modules (IGBT), Microprocessors and Microwave Power Modules. The heat flux that needs to be dissipated from small areas in these equipment can be very high. For example, Karayiannis and Mahmoud [1] reported that the chip local heat flux can reach up to 50 MW/m^2 in IGBT modules. These high heat fluxes motivated researchers in academia and industry to propose and test innovative cooling techniques to meet the high heat fluxes encountered in these applications. Currently, several techniques can be adopted in the thermal management of electronic equipment such as heat pipes, thermoelectric modules, vapour chambers, single-phase liquid cooling loops, vapour compression refrigeration cycles, spray and liquid jet impingement and immersion cooling. For example, water single-phase flow is currently used in cooling the Summit computer data centre, which consists of 4608 nodes (power AC922 server) and each node has two IBM POWER9 CPUs and six NVIDIA Tesla V100 GPUs [2]. These cooling techniques have some restrictions and are not able to meet the current and future thermal demand (high/ultra-high heat fluxes) in the aforementioned applications. Two-phase flow boiling in microchannel heat sinks can be used in electronics cooling instead of single-phase liquid loops due to the possible higher heat transfer coefficients, possible uniform substrate temperature and lower fluid charge. However, the design of multi-microchannel evaporators still requires full understanding of the effect of many parameters that affect flow boiling in confined spaces. Accordingly, further research is required to elucidate the effect of mass and heat flux, channel geometry and material on flow boiling regimes, pressure drop and heat transfer rates in these micro-evaporators that can lead to adoption of this technology by industry.

* Correspondence to Prof. Tassos G. Karayiannis, Department of Mechanical and Aerospace Engineering, Brunel University London, Uxbridge, Middlesex, UB8 3PH, UK. Tel: +44 (0) 1895 267132, Fax: +44 (0)1895 256392
E-mail address: tassos.karayiannis@brunel.ac.uk (T.G. Karayiannis).

https://doi.org/10.1016/j.ijheatmasstransfer.2022.123101

Nomenclature

A	area, (m^2)
b	thickness of the heat sink base, (m)
C	dimensionless correction factor, (-)
c_p	specific heat at constant pressure, (J/kg K)
D_h	hydraulic diameter, (m)
f	Fanning friction factor, (-)
G	mass flux, (kg/m^2s)
H	height, (m)
h	heat transfer coefficient, (W/m^2 K)
$\bar{h}$	average heat transfer coefficient, (W/m^2 K)
i	specific enthalpy, (J/kg)
i_{lg}	latent heat of vaporization, (J/kg)
k	thermal conductivity, (W/m K)
K_∞	dimensionless incremental pressure drop number, (-)
L	length, (m)
L^*	dimensionless length, (-)
m	fin parameter, (-)
$\dot{m}$	mass flow rate, (kg/s)
N	number of channels, (-)
NSD	nucleation site density, (n/m^2)
$\overline{Nu}$	average Nusselt number, (-)
P	pressure, (Pa)
Pr	Prandtl number, (-)
Q	heat rate or power, (W)
q''	heat flux, (W/m^2)
R	thermal resistance, (K/W)
Ra	average surface roughness, (μm)
Re	Reynolds number, (-)
T	temperature, (K)
v	specific volume, (m^3/kg)
W	width, (m)
x	vapour quality, (-)
y	distance between thermocouple and channel bottom, (m)
Z	axial distance, (m)

Greek Symbols

α	area ratio, void fraction, (-)
β	aspect ratio, (-), $\beta = W_{ch}/H_{ch}$
γ	surface-liquid interaction parameter, (-)
ΔP	pressure drop, (Pa)
ΔT	temperature difference, (K)
η	fin efficiency, (-)
θ	dimensionless surface roughness parameter, (-)
ρ	density, (kg/m^3)
σ	surface tension, (N/m)

Subscript

acc	acceleration
app	apparent
b	base
c	cooling
cd	conductive
ch	channel
cv	convetive
exp	experimental
f	fluid
FD	fully developed
fin	channel fin
fr	frictional
g	gas or vapour
ht	heat transfer
i	inlet
l	liquid
lg	Liquid to vapour
m	metal
max	maximum
meas	measurment
min	minimum
o	outlet
p	pump
sat	saturation
sc	sudden contraction
se	sudden expansion
sp	single-phase
sub	subcooled
sup	superheat
th	thermocouple
tot	total
tp	two-phase
w	wall
wi	internal wall surface
z	axial local

The choice of appropriate heat sink material is considered an essential step in the thermal design of micro-evaporators, with copper, being on the list of choices. This is because copper has high thermal conductivity, easy malleability, machinability and is recyclable. However, copper heat sinks have some drawbacks such as cost, weight and corrosion. Indeed, the answer to this question will be more complicated when a small-scale thermal management system is considered. It is known that heat sinks with different surface materials will have different thermal conductivity, surface texture and wettability. These parameters may affect flow boiling characteristics especially in micro-scale configurations, which have yet to be fully understood. This can be seen in the large discrepancy among many empirical correlations and models that were proposed in the literature for the prediction of two-phase flow patterns, pressure drop and heat transfer coefficient at this scale. The effect of surface material, surface roughness and wettability are discussed in the following sub-sections.

1.1. Effect of material

To the best of the authors' knowledge, only a small number of researchers studied the effect of channel material on flow boiling in small to micro passages. Bang and Choo [3] examined flow boiling of R-22 in copper, aluminium and brass tubes with inner diameter of 1.67 mm at a fixed mass flux of 600 kg/m^2 s and vapour quality up to 0.9. They mentioned that the effect of surface material on the heat transfer coefficient was small. Pike-Wilson and Karayiannis [4] tested R-245fa in copper, brass and stainless steel vertical tubes with diameter 1.1 mm. Their results showed that the effect of material was not significant when the local vapour quality was less than 0.35. However, at qualities above 0.35, brass and stainless-steel tubes had higher heat transfer coefficient than the copper tube. They concluded that the material itself did not have a significant influence on the heat transfer coefficient and different surface roughness and characteristics of the three tested tubes could account for this difference. They also reported that, for the tested fluid, annular flow was the dominant flow pattern in all tubes. In addition, the two-phase pressure drop in the brass tube was the highest, while the stainless steel tube provided the lowest pressured drop. Vandervort et al. [5] examined the effect of material on the critical heat flux for water flow boiling in metal-

lic tubes with inner diameter 0.3–2.7 mm, made of stainless steel (with different grades), nickel, brass and Inconel 600. They found that the effect of surface material on the CHF was insignificant. In some of the work above, varying the material may result in different surface roughness and thus it may be difficult to separate the effect of the two factors, i.e. roughness and material. The insignificant effect of material reported above by researchers may be due to the fact that the tested tubes are thin-wall tubes, i.e. no big difference in the material heat capacity or thermal inertia. In microchannel heat sinks, the channels are usually machined/cut on a thick metal plate. Thus, the material heat capacity might have an effect in multi-microchannel evaporators.

1.2. Effect of surface roughness

Jones and Garimella [6] tested the effect of roughness on flow boiling of deionized water in copper microchannel heat sinks with 0.5 × 0.5 mm cross section. They used two manufacturing methods to vary the surface roughness namely, saw-cutting and electrical discharge machining. The obtained average surface roughness was found to be 1.4, 3.9 and 6.7 μm. It was found that, at heat fluxes less than 700 kW/m^2, the effect of surface roughness on the heat transfer coefficient was small. In contrast, at higher heat fluxes, the surfaces with 3.9 and 6.7 μm roughness exhibited higher heat transfer coefficient than the surface with 1.4 μm roughness. Moreover, the pressure drop was high in the roughest surface (Ra = 6.7 μm) and low in the smoothest one (Ra = 1.4 μm). Alam et al. [7] studied flow boiling of deionized water in silicon micro-gap heat sink. They modified the surface to obtain average roughness of 0.6, 1.0 and 1.6 μm. It was found that the heat transfer coefficient and nucleation site density increased with increasing surface roughness, while the effect of roughness on pressure drop was insignificant. Jafari et al. [8] investigated flow boiling of R134a in rectangular microchannels having channel height and width of 0.7 and 0.25 mm, respectively. They tested three copper heat sinks having different surface roughness of 0.21, 0.96 and 2.38 μm. Their results showed that the heat transfer coefficient and the pressure drop increased with increasing surface roughness.

Different surface finish could result in different surface microstructures (surface characteristics), which include deposits, flakes, debris, cracks and scratches as reported in the literature. The geometry of surface cavities (possible nucleation sites) is an important parameter and should be considered in discussing the effect of surface characteristics rather than simply the average surface roughness. This is because different surface profiles may show similar surface average roughness, see [9]. The different surface microstructure may define the size and number of nucleation sites, which could affect the flow boiling characteristics. Karayiannis et al. [10] examined flow boiling of R134a in vertical stainless steel tubes with 1.1 mm inner diameter and reported different heat transfer results due to difference in surface microstructure. They tested seamless cold drawn and welded tubes. The SEM images indicated that the surface of the welded tube is extremely smooth compared to the cold drawn tube. The welded tube showed that the local heat transfer coefficient varied significantly along the tube, without a clear and as expected increasing trend with heat flux. In contrast, the cold drawn tube showed an increase in the heat transfer coefficient with heat flux with a small variation along this tube. They attributed this to the existence of a higher number of nucleation sites on the cold drawn tube.

1.3. Effect of wettability

Different fluid-surface combinations can result in different contact angles, i.e. wettability, with fluid-surfaces identified as tending to be hydrophobic (contact angles greater than 90°) and hydrophilic (contact angles less than 90°). Vontas et al. [11] carried out a numerical study using ethanol in a stainless steel channel having 0.2 mm hydraulic diameter. Different ranges of dynamic contact angle were tested (from 19 to 120° for the advancing and 8–15° for the receding contact angle). They reported that slug flow occurred at all conditions while churn flow was only formed at low mass flux and high heat flux. Their results showed that, the hydrophilic surfaces exhibited slightly higher heat transfer rate compared to the hydrophobic surfaces. This was attributed to the dominance of liquid film evaporation in the hydrophilic surfaces while evaporation was only restricted to the three-phase contact line in the hydrophobic surfaces. Ahmadi and Okawa [12] carried out an experimental investigation on sub-cooled boiling of deionized water in a vertical copper channel with dimensions of 10 × 20 mm at a fixed mass flux of 400 kg/m^2 s and pressure 100–400 kPa. The surface wettability was modified by different degrees of surface oxidation and the static contact angle was 18, 57, 94 and 97°. It was found that at the onset of nucleate boiling, the bubbles stayed attached to the surface on the hydrophobic surfaces with fluctuations in size. In contrast, the bubbles were found to depart their nucleation sites on the hydrophilic surfaces, i.e. lift-off and slide along the surface. Additionally, at the onset of nucleate boiling, the nucleation site density was found to decrease with increasing surface wettability, i.e. larger number of bubbles on the hydrophobic surfaces. Choi et al. [13] conducted an experimental investigation of water flow boiling in glass rectangular microchannels with 0.5 mm hydraulic diameter and contact angle of 25 and 105°. It was reported that the hydrophobic surfaces achieved higher heat transfer coefficients compared to the hydrophilic surfaces. The authors attributed this to the higher number of active nucleation sites and the liquid film motion. They also found that the hydrophobic surfaces provided higher pressure drop [14]. Tan et al. [14] carried out a numerical study using a silicon micro-tube with 0.6 mm inner diameter and water with contact angle of 40 and 120° plus a wettability gradient along the tube from 120–40°. They demonstrated that the effect of surface wettability on the heat transfer coefficient can vary according to the flow patterns and mass flux range. Bubbly, confined bubble and slug flow were identified at wall heat flux of 150 kW/m^2 and mass flux of 140, 280 and 560 kg/m^{2}s. Trieu et al. [15] conducted an experimental study using water in a rectangular channel. The channel height, width and length were 0.5, 5 and 180 mm, respectively. Four different static contact angles were tested namely 26, 49, 63 and 104°. They found that the two-phase pressure drop increased with increasing contact angle, i.e. with average difference of 170% between the 104° and the wetting surface with a contact angle of 26°. They noted that the higher surface tension force of the high contact angle surface could maintain the bubbles on the channel surface leading to higher frictional pressure drop.

As disused above, the effect of surface material on the flow boiling characteristics in mini and microchannels was not widely studied and conclusively or clearly understood. Channel surfaces made of high thermal conductivity material do not always show better thermal performance. Different surface microstructure – not always identified using the average surface roughness parameter alone - could play a significant effect on flow boiling characteristics. The number and size of active surface cavities per unit area is increasing in importance as the passage size decreases. The fluid-surface combination resulting in different contact angles can also be an important parameter. The present study aims to investigate the thermal performance of two heat sinks made of two different metals, i.e. copper and aluminium, in flow boiling of HFE-7100 in multi-microchannels with channel hydraulic diameter of 0.46 mm. The thermophysical properties of this eco-friendly and dielectric refrigerant obtained from EES software at atmospheric pressure are presented in Table 1. All experiments were carried out at 1 bar sys-

Table 1
Thermophysical properties of HFE-7100 at 1 bar obtained from EES software.

[J/kg]	ρ_l[kg/m^3]	ρ_g[kg/m^3]	k_f[W/mK]	cp[J/kgK]	σ[N/m]
111661	1373	9.575	0.06206	1157	0.0136

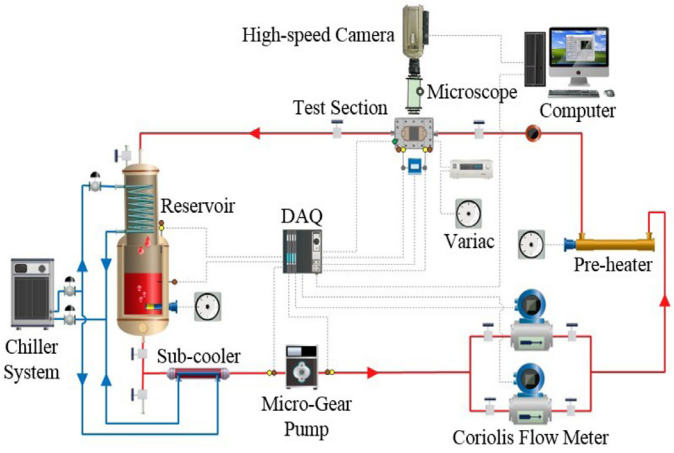

Fig. 1. Experimental facility [16].

tem pressure, 5 K inlet sub-cooling, 50-250 kg/m^{2}s mass flux and wall heat flux up to 174 kW/m^2.

2. Experimental system

2.1. Experimental rig

The experimental study was conducted using the rig depicted in Fig. 1 and described in detail in [16,17]. The rig consisted of a 9-litter liquid reservoir, tube-in-tube sub-cooler, micro-gear pump, two Coriolis flow meters, pre-heater with 1500 W, DAQ-system (National Instruments) with a frequency of 1 kHz, cooling coil condenser and the test section. A chiller system with cooling capacity of 2.9 kW was also connected to the rig to reject the heat from the reservoir and the sub-cooler. The cooling coil and the immersion heater were placed inside the reservoir to control the system pressure during the experiments and to help conduct the degassing process. Moreover, the pre-heater was used to control the fluid inlet sub-cooling at the test section. A digital driver was connected to the micro-gear pump to adjust the flow rate. This pump can supply flow rate up to 2,304 ml/min. Two Coriolis flow meters (for low and high mass flow rates) with accuracy of ±0.1% were used to measure the flow rate. Three Variac transformers were connected to the reservoir, the pre-heater and the test section in order to adjust the supplied power. A power meter, model Hameg HM8115-2 with accuracy of ±0.4%, was connected to the test section to measure the input power. A set of measuring sensors, such as thermocouples and pressure transducers, were mounted at different locations in the rig. These sensors in addition to the flow meters were connected to the DAQ-system and then to the computer. LabView software was installed and used to record all the measuring signals during the experiments. In this study, two-phase flow patterns were captured using a Phantom high-speed camera (1000 fps at 512 × 512 pixel) coupled with an LED lighting system and Huvitz HSZ-645TR microscope.

2.2. Cooper and aluminum test sections

The test section consisted of four main parts, namely the bottom plate, the housing, the cover plate and the heat sink block, see Fig. 2 and [16]. The housing and the bottom plate were made of a Polytetrafluoroethylene block to minimize the heat loss. The cover plate was manufactured using a transparent polycarbonate sheet to allow flow visualisation. This plate also included both the inlet and outlet plena, with a semi-circular shape. It also included four tapping holes to insert the inlet/outlet fluid thermocouples, inlet/outlet pressure transducers and the differential pressure transducer ports, see Fig. 2(b). The cover plate was placed on the topside of the housing. An O-ring was inserted between the cover plate and the heat sink block to prevent fluid leakage. The heat sink block was designed and manufactured with width, length and height of 26, 51 and 94.5 mm, respectively, as shown in Fig. 3(a). This block included multi-microchannels on the topside and four vertical holes at the bottom side. These holes were used to insert four cartridge heaters having total heating power of 700 W. Twelve K-type thermocouples were inserted into this block. These thermocouples were used to assess the temperature distribution along the microchannels, in the vertical and transverse direction. All heat transfer calculations were computed along the channels at three locations, i.e. three thermocouples were inserted underneath and along the channels. Furthermore, five of the vertical thermocouples were used in the measurement of the base heat flux and to help confirm that there was 1D heat conduction in the vertical direction.

A high-precision milling machine, model Kern HSPC-2216, was used to fabricate the two heat sinks of copper and aluminium with similar channel dimensions. The microchannels and the inlet and outlet plena with semi-circular shape were milled on the top surface of the heat sink block as shown in Fig. 3(b). Thirty six horizontal square multi-microchannels were fabricated with a channel height and width of 0.46 mm and a separating fin width of 0.1 mm. An optical coordinate measuring machine, model TESA-VISIO 200GL, with an accuracy of ±2 μm was used to measure all the channel dimensions. These microchannels had a total base area of 20 mm width times 25 mm length. The average surface roughness of the channel bottom was measured using Zygo NewView 5000. This value (the average value at three different locations) was found to be 0.286 and 0.192 μm for copper and aluminium channels, respectively.

Oxygen-free copper block having a thermal conductivity of 390 W/mK at 25°C was chosen. It is worth mentioning that there are many aluminium grades that can be used in industrial applications. However, the grades 6060, 6061 and 6063 are most commonly used in heat exchangers and heat sinks [18]. Accordingly, 6063 aluminium alloy with 204 W/mK thermal conductivity at 25°C was chosen in the present study. It was decided to examine the thermal performance of aluminium heat sink instead of other metals due to the following reasons: (i) Light weight; the weight of the present microchannel heat sink, without the heating block, is 22.4 and 6.8 g for copper and aluminium, respectively, i.e. a reduction of about 70% which may be a required criterion for some applications in electronics cooling. (ii) Low cost; the metal price/kilogram of aluminium is roughly £2.25, while this increases to £7.02 for copper (see: www.dailymetalprice.com). (iii) Low aging factor; microchannel heat sinks made of copper are expected to show deterioration in flow boiling heat transfer during long-running operations due to oxidation [19]. However, aluminium can create a protection layer, i.e. alumina, on the surface.

Different surface materials may result in different surface microstructures that may affect the thermal performance of any heat sink. Therefore, a Scanning Electron Microscope, model LEO 1455VP, was used to conduct a SEM analysis for both channel bottom surfaces. Fig. 4 depicts the SEM images taken at a magnification of 2000X. It can be seen that although the same machining conditions were used during the manufacturing process, the aluminium surface was different compared to that of copper. The aluminium surface had different and more cutting marks than those

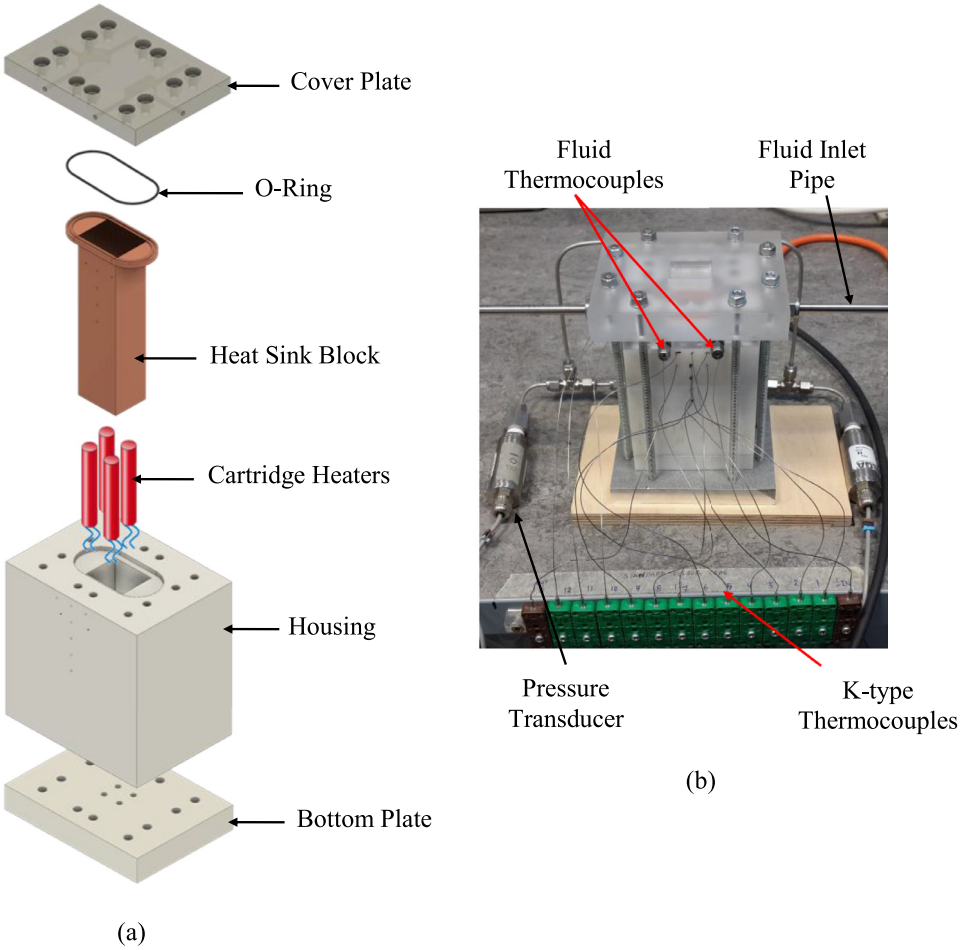

Fig. 2. Test section: (a) Exploded drawing [16] (b) Photograph of the test section.

on the copper surface. Different marks may lead to different surface peaks and valleys. Moreover, more debris and a higher number of cavities were found on the aluminium surface compared to copper. Fig. 4(b) shows that the cavity mouth size of aluminium looks larger than those of copper. Different material properties may lead to these differences in the surface microstructure. This may play a significant role in flow boiling characteristics especially in micro-scale geometries.

3. Data reduction

3.1. Single-phase flow

The local single-phase heat transfer coefficient was calculated as follows:

$$h_{sp(z)} = \frac{q''_w}{\left(T_{wi(z)} - T_{f(z)}\right)} = \frac{q''_b(W_{ch} + W_{fin})}{\left(T_{wi(z)} - T_{f(z)}\right)(W_{ch} + 2\eta H_{ch})} \tag{1}$$

where q''_w, q''_b, H_{ch}, W_{ch}, W_{fin}, $T_{wi(z)}$, $T_{f(z)}$ and η are the wall heat flux, base heat flux, the channel height, the channel width, the fin width, the local inner surface temperature, the local fluid temperature and the fin efficiency, respectively. The wall heat flux is based on the total active heat transfer surface area (A_{ht} , see equation 8 below) and the base heat flux on the length of the channels times the total microchannel width (25 mm x 20 mm). The base heat flux was estimated from the measured vertical wall temperature gradient as given by Eq. (2) below

$$q''_b = -k_m \left.\frac{dT}{dy}\right|_{y=0} \tag{2}$$

where k_m is the metal thermal conductivity. The fin efficiency in Eq. (1) was calculated using Eq. (3) and (4) below.

$$\eta = \frac{\tanh(mH_{ch})}{mH_{ch}} \tag{3}$$

$$m = \sqrt{\frac{2h_{(z)}}{k_m W_{fin}}} \tag{4}$$

$h_{(z)}$ is the heat transfer coefficient (single or two-phase, as the case might be). The local surface inner temperature was calculated using Eq. (5), while the local fluid temperature was found using Eq. (6).

$$T_{wi(z)} = T_{th(z)} - \frac{q''_b y}{k_m} \tag{5}$$

$$T_{f(z)} = T_{fi} + \frac{q''_b W_b z}{\dot{m} c_{pl}} \tag{6}$$

$T_{th(z)}$ and y are the local thermocouple temperature and the vertical distance between the topmost thermocouple and the channel bottom, respectively. The average Nusselt number $\overline{Nu}$ was calculated using Eq. (7).

$$\overline{Nu} = \frac{1}{L_{ch}} \int_0^{L_{ch}} \frac{h_{sp(z)} D_h}{k_l} dz \tag{7}$$

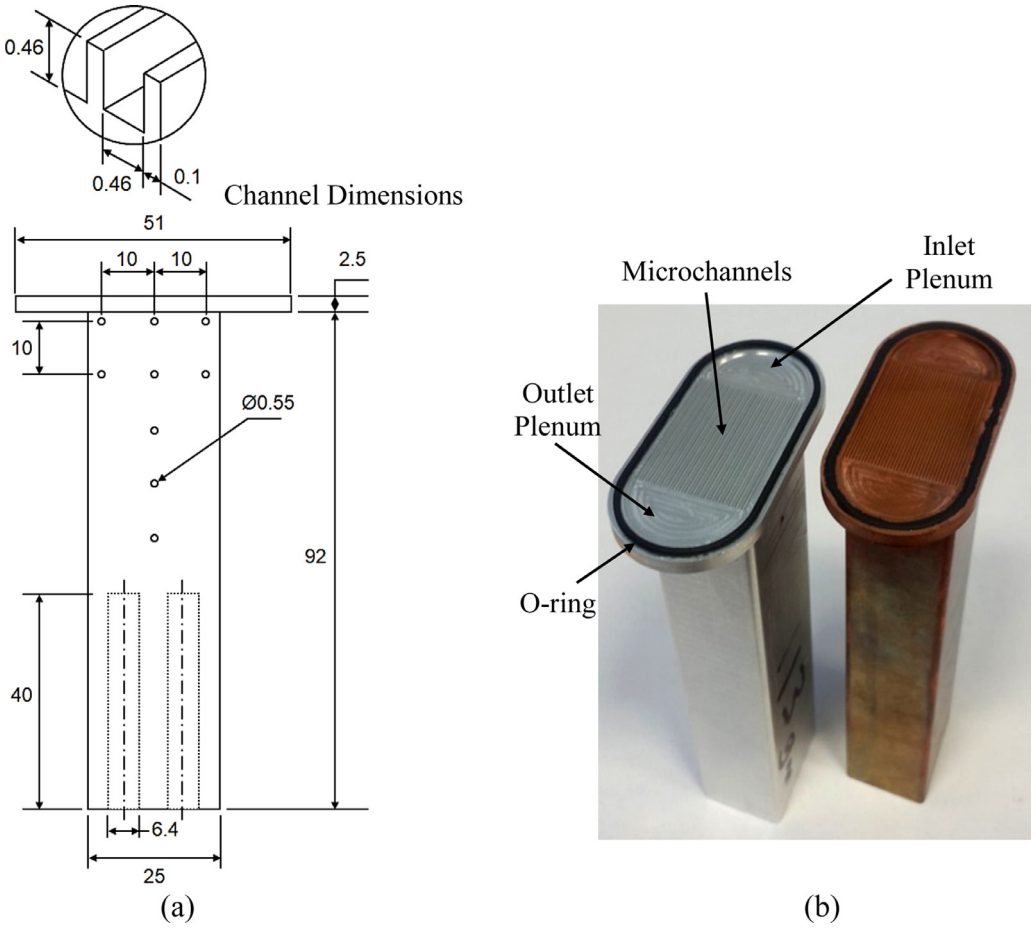

Fig. 3. Heat sink block, dimensions in mm: (a) Schematic diagrame (b) Photograph.

where D_h and k_l are the channel hydraulic diameter and the liquid thermal conductivity, respectively. The total heat transfer area A_{ht} was calculated using Eq. (8) for a three-side heated channel, i.e. adiabatic cover plate.

$$A_{ht} = (2H_{ch} + W_{ch})L_{ch}N \tag{8}$$

L_{ch} and N are the channel length and the number of channels, respectively. The channel mass flux was obtained by assuming equal flow distribution among the channels as follows:

$$G_{ch} = \frac{\dot{m}}{H_{ch}W_{ch}N} \tag{9}$$

The experimental single-phase Fanning friction factor was calculated using Eq. (10) while the channel pressure drop was calculated from Eq. (11),

$$f_{exp} = \frac{\Delta P_{ch} D_h}{2L_{ch}\nu_l G_{ch}^2} \tag{10}$$

$$\Delta P_{ch} = \Delta P_{meas} - (\Delta P_{sc} + \Delta P_{se}) \tag{11}$$

where ΔP_{meas}, ΔP_{sc}, and ΔP_{se} are the total measured pressure drop, the sudden contraction pressure drop at the channel inlet, and the sudden expansion pressure drop at the channel outlet, respectively. The total pressure drop was measured directly from the differential pressure transducer, while other components were calculated as follows, see Remsburg [20]:

$$\Delta P_{sc} = \frac{1}{2}G_{ch}^2\nu_l\left[1 - \alpha^2 + 0.5(1-\alpha)\right] \tag{12}$$

$$\Delta P_{se} = \frac{1}{2}G_{ch}^2\nu_l\left[\frac{1}{\alpha^2} - 1 + (1-\alpha)^2\right] \tag{13}$$

where α is the area ratio, $\alpha = \frac{A_{min}}{A_{max}} = \frac{H_{ch}W_{ch}N}{H_{ch}W_b} = \frac{7.6}{9.2} = 0.83$.

3.2. Two-phase flow

The local two-phase heat transfer coefficient was calculated from Eq. (14):

$$h_{tp(z)} = \frac{q''_b(W_{ch} + W_{fin})}{\left(T_{wi(z)} - T_{sat(z)}\right)(W_{ch} + 2\eta H_{ch})} \tag{14}$$

The local saturation temperature $T_{sat(z)}$ was found from the corresponding local pressure, see Eq. (15), by assuming a linear pressure drop along the channels.

$$P_{sat(z)} = P_{sat(z,sub)} - \left(\frac{z - L_{sub}}{L_{ch} - L_{sub}}\right)\Delta P_{tp} \tag{15}$$

where $P_{sat(z,sub)}$, z, L_{sub} and ΔP_{tp} are the local saturation pressure at the end of the single-phase region, the axial distance, the single-phase length and the two-phase pressure drop, respectively. The two-phase pressure drop ΔP_{tp} was calculated by subtracting the single-phase pressure drop from the channel pressure drop as follows:

$$\Delta P_{tp} = \Delta P_{ch} - \Delta P_{sp} \tag{16}$$

The channel pressure drop ΔP_{ch}in the two-phase flow was calculated using Eq. (11), as mentioned above, but after replacing Eq. (13) for the sudden enlargement at the channel outlet in single-phase flow with Eq. (17) below for two-phase flow, from Collier and Thome [21]

$$\Delta P_{se} = G_{ch}^2\alpha(1-\alpha)\nu_l\left[1 + \frac{\nu_{lg}}{\nu_l}x_o\right] \tag{17}$$

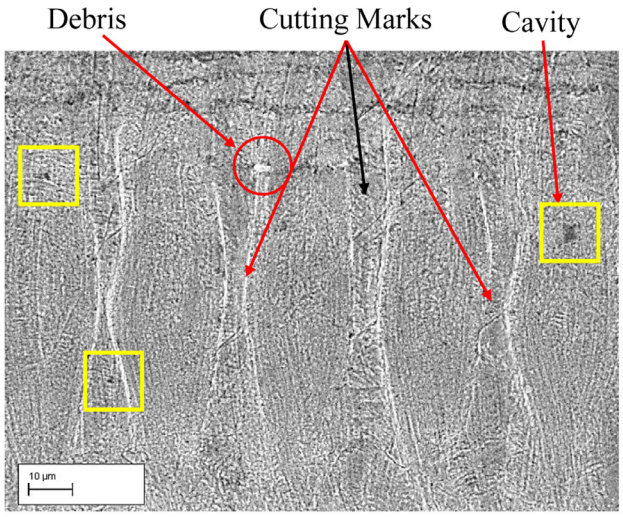

Fig. 4. Topography images of the channel bottom from SEM at a magnification of 2000X and scan area of 0.105 × 0.14 mm: (a) Copper (b) Aluminium. Red circles: debris. Yellow squares: cavities.

where v_{lg} is the difference in specific volume between vapour and liquid and x_o is the vapour quality at the channel exit. The local saturation pressure at the end of the single-phase region was calculated using Eq. (18), while the single-phase length was obtained from Eq. (19).

$$P_{sat(z,sub)} = P_i - \frac{2 f_{app} G_{ch}^2 L_{sub}}{\rho_l D_h} \tag{18}$$

$$L_{sub} = \frac{\dot{m} c_{pl} \left(T_{sat(z,sub)} - T_{fi}\right)}{q''_b W_b} \tag{19}$$

The apparent Fanning friction factor f_{app} for developing laminar flow was calculated from Eq. (20) proposed by Shah and London [22] as follows:

$$f_{app} = \frac{3.44}{Re\sqrt{L^*}} + \frac{f_{FD}Re + \frac{K_\infty}{4L^*} - 3.44/\sqrt{L^*}}{Re\left(1 + C(L^*)^{-2}\right)} \tag{20}$$

$$L^* = L_{sub}/ReD_h \tag{21}$$

$$f_{FD}Re = 24\left(1 - 1.355\beta + 1.946\beta^2 - 1.7012\beta^3 + 0.9564\beta^4 - 0.2537\beta^5\right) \tag{22}$$

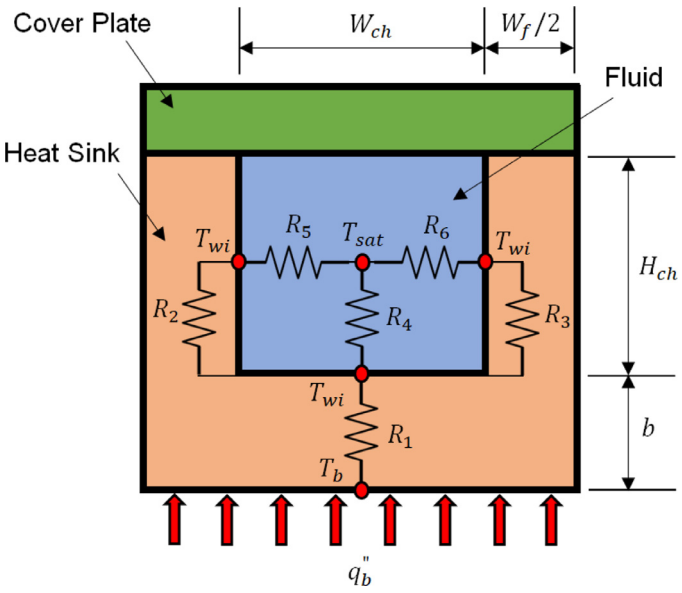

Fig. 5. Schematic diagrame of thermal resistance network for a single channel and half fin [not to scale].

where K_∞, C, β and L^* are the dimensionless incremental pressure drop number, the dimensionless correction factor, the channel aspect ratio and the dimensionless length, respectively. The dimensionless incremental pressure drop number and the dimensionless correction factor were obtained from Shah and London [22]. It can be seen from Eq. (18) that an iteration process should be conducted between Eq. (18) and (19) to find the local saturation pressure at the end of the single-phase region and the single-phase length. The local vapour quality was calculated using Eq. (23) below.

$$x_{(z)} = \frac{i_{(z)} - i_{l(z)}}{i_{\mathrm{lg}\,(z)}} \tag{23}$$

where $i_{(z)}$, $i_{l(z)}$ and $i_{\mathrm{lg}(z)}$ are the local specific enthalpy, the local liquid specific enthalpy and the local latent heat of vaporization, respectively. The local specific enthalpy was calculated from an energy balance as follows:

$$i_{(z)} = i_i + \frac{q''_b W_b z}{\dot{m}} \tag{24}$$

The average two-phase heat transfer coefficient along the channels was calculated using Eq. (25) below.

$$\bar{h}_{tp} = \frac{1}{L_{ch} - L_{sub}} \int_{L_{sub}}^{L_{ch}} h_{(z)} dz \tag{25}$$

In order to compare the thermal performance of the tested heat sinks, the total thermal resistance was calculated using the schematic depicted in Fig. 5 for a single microchannel and half fin on both sides. It was assumed that the fluid saturation temperature is uniform along the channel cross section. It can be seen that six thermal resistances are included in the schematic namely; three conduction resistances (R_1, R_2 and R_3) across the channel base and the fins and three convection resistances (R_4, R_5 and R_6) between the fluid and the bottom and side walls. The definition of each thermal resistance is given below as:

$$R_1 = \frac{b}{k_m\left(W_{ch} + W_{fin}\right)L_{ch}N} \tag{26}$$

$$R_2, R_3 = \frac{H_{ch}}{k_m (W_{fin}/2) L_{ch} N} \tag{27}$$

$$R_4 = \frac{1}{\bar{h} W_{ch} L_{ch} N} \tag{28}$$

$$R_5, R_6 = \frac{1}{\bar{h} H_{ch} L_{ch} N} \tag{29}$$

Thus, the total thermal resistance can be calculated as:

$$R_{tot} = R_1 + \left[\frac{1}{R_4} + \frac{1}{R_2 + R_5} + \frac{1}{R_3 + R_6} \right]^{-1} \tag{30}$$

$$R_{tot} = \frac{b}{k_m \left(W_{ch} + W_{fin} \right) L_{ch} N} + \left[\eta \bar{h} W_{ch} L_{ch} N + \frac{2}{\frac{H_{ch}}{k_m \left(0.5 W_{fin} \right) L_{ch} N} + \frac{1}{\eta \bar{h} H_{ch} L_{ch} N}} \right]^{-1} \tag{31}$$

It is worth mentioning that, the thermal conductivity of each heat sink material was estimated at the fluid saturation temperature, e.g. 394.6 W/mK for copper and 200.8 W/mK for aluminium. Additionally, the fin efficiency was taken as 0.95 (based on the experimental data, the fin efficiency was equal or greater than 0.95). Eq. (32) below is a simplified form that can be used to calculate the total thermal resistance if the conduction resistance in the fins is ignored.

$$R_{tot} = R_{cd} + R_{cv} \tag{32}$$

$$R_{cd} = \frac{b}{k_m W_b L_{ch}} \tag{33}$$

$$R_{cv} = \frac{1}{\bar{h} (2\eta H_{ch} + W_{ch}) N L_{ch}} \tag{34}$$

$\bar{h}$ is the average heat transfer coefficient (including single and two-phase components) as defined in Eq. (35). The thickness b of the heat sink base is 2 mm.

$$\bar{h} = \frac{1}{L_{ch}} \int_0^{L_{ch}} h_{(z)} dz \tag{35}$$

In the present study, the calculation based on all resistances (Eq. (31)) and the simplified form (Eq. (32)) were compared against each other. The cooling load Q_c was calculated using Eq. (36).

$$Q_c = q''_b A_b \tag{36}$$

The energy consumption by the pump was calculated from Eq. (37).

$$Q_p = \frac{\dot{m} \Delta P_{meas}}{\rho_l} \tag{37}$$

The acceleration and frictional pressure drop components were calculated in the current study to assess the contribution of each component to the total two-phase pressure drop. The acceleration pressure drop component was calculated using Eq. (38) and Eq. (39) for the void fraction proposed by [23].

$$\Delta P_{acc} = G^2 \nu_l \left[\frac{x_o^2}{\alpha_o} \left(\frac{\nu_g}{\nu_l} \right) + \frac{(1 - x_o)^2}{1 - \alpha_o} - 1 \right] \tag{38}$$

$$\alpha_o = \left[1 + \frac{1 - x_o}{x_o} \left(\frac{\nu_l}{\nu_g} \right)^{0.67} \right]^{-1} \tag{39}$$

The frictional pressure drop component was calculated as follows:

$$\Delta P_{fr} = \Delta P_{tp} - \Delta P_{acc} \tag{40}$$

Table 2
Experimental uncertainties.

Parameter	Uncertainty
Temperature T-type	±0.02K
Temperature K-type	±0.04–0.1K
Inlet pressure transducer	±0.5kPa
Outlet pressure transducer	±0.4kPa
Differential pressure	±0.08%
Coriolis mass flow rate	±0.1%
Fanning friction factor	±1.6–2.2%
Average Nusselt number	±1.3–4%
Local vapour quality	±0.3–15%
Local heat transfer coefficient	±0. 2–11%
Mass flux	±0.3–0.6%
Heat flux	±0.12–3.2%

Table 3
Experimental operating conditions.

System pressure [bar]	1
Saturation temperature [°C]	59.63
Inlet sub-cooling [K]	5
Mass flux [kg/m^{2}s]	50–250
Wall heat flux [kW/m^2]	9.5 to 174
Exit vapour quality [-]	0 to 0.99

In the present study, the uncertainty of the measured variables were calculated from the calibration procedure, while the uncertainties of all derived variables were calculated using a procedure proposed by Coleman and Steele [24]. All the experimental uncertainties are presented in Table 2.

4. Experimental procedure and single-phase validation

Single-phase flushing and degassing processes were conducted at different operating conditions during this study. These steps were carried out before starting any two-phase flow experiment to remove any trapped gases in the system and help ensure appropriate validation of the experimental rig. More details are given in Al-Zaidi et al. [17,25]. In the two-phase flow experiments, HFE-7100 was tested at a system pressure of 1 bar, inlet sub-cooling of 5 K and five mass fluxes, namely: 50, 100, 150, 200 and 250 kg/m^{2}s. The supplied heat at the test section was increased gradually until the exit vapour quality reached near one. The experimental operating conditions are presented in Table 3. All the measured data were collected for two minutes using LabView software when the system became steady. Steady state condition was assumed when the variation in the measuring signals (temperature, mass flow rate and pressure) were very small, i.e. less than 5% in the fluctuation of the measuring signals. The average values of these data were then taken and used in the EES software to calculate all the necessary parameters reported in the above data reduction section. The software was also adopted to find all the thermophysical properties of the examined fluid. Flow visualization was captured for each run at three locations along the heat sink (near the entry, middle and near the exit). All the recorded videos were then converted to image sequences using the Phantom camera control software in order to identify and study the features of flow patterns.

Single-phase experiments were carried out before conducting two-phase flow experiments in order to check the validation of the experimental system. The experimental Fanning friction factor versus Reynolds number was calculated and shown in Fig. 6. This figure is presented for the aluminium heat sink using adiabatic experiments. The experimental results were compared with the correlation by Shah and London [22] for developing flow. A good agreement was found between the experimental results and the correlation with a mean absolute error of 8%. Single-phase heat transfer experiments were also conducted to calculate the aver-

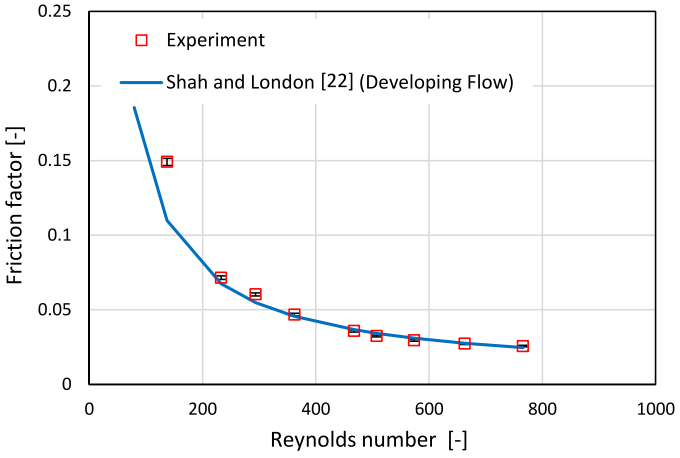

Fig. 6. Experimental Fanning friction factor versus Reynolds number for aluminium heat sink.

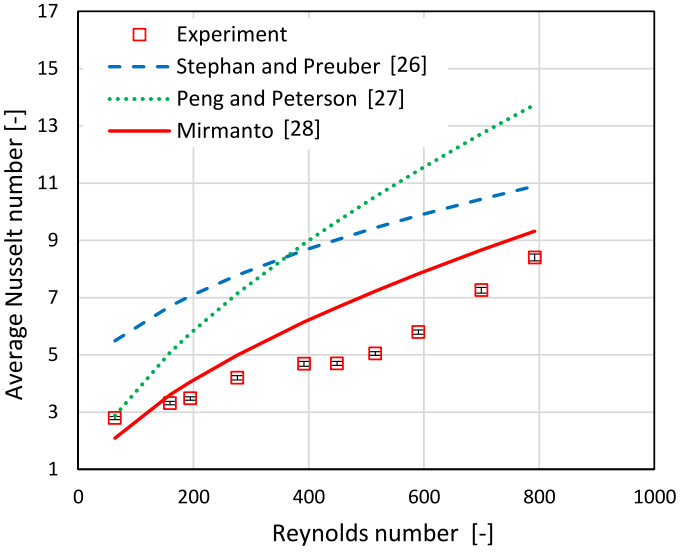

Fig. 7. Average Nusselt number versus Reynolds number for the aluminium heat sink.

age Nusselt number. This was plotted versus Reynolds number and compared with the correlations of Stephan and Preuber [26], Peng and Peterson [27] and Mirmanto [28], as shown in Fig. 7. It can be seen that there was a reasonable agreement with the correlation by Mirmanto [28] giving a mean absolute error less than 25%. This good agreement could be due to the fact that this correlation was proposed for a rectangular channel having an adiabatic cover plate and was heated from the bottom by cartridge heaters block (partly heated channel), i.e. similar to the current study. It is worth mentioning that this good agreement was also found when the copper heat sink was tested, see also [17]. There is disagreement between the experimental data and refs. [26,27]. The work described in [26] is for circular channels, hence a possible reason for this disagreement. The work in [27] was based on rectangular channels, i.e. an empirical equation based on specific data. The disagreement between the current experimental data and [27] could be due to the following reasons: (1) longer channels in [27] compared to shorter channels in the current study (developing versus developed flow), (2) In [27], the channels were made of stainless steel, i.e. low thermal conductivity, (3) the channels tested in [27] have very thick fins (2 – 4.5 mm compared to 0.1 mm in the present study) and (4) direct electric heating to a thin plate was used in [27] compared to heating a copper block by cartridge heaters in the present study. This combined with the low thermal conductivity of stainless steel can affect the thermal boundary conditions, i.e. constant heat flux in [27] versus constant temperature boundary condition in the present study due to the high thermal conductivity of copper and aluminium. The repeatability of the two-phase flow results was also assessed as shown in Fig. 8. One experiment was repeated after twenty days using the same operating conditions. It can be seen that there were only minor deviations in the reliability of these two data sets with a mean absolute error of 4.65 %. The abovementioned discussion demonstrates that the experimental system is valid and can be used to provide accurate results for the two-phase flow experiments.

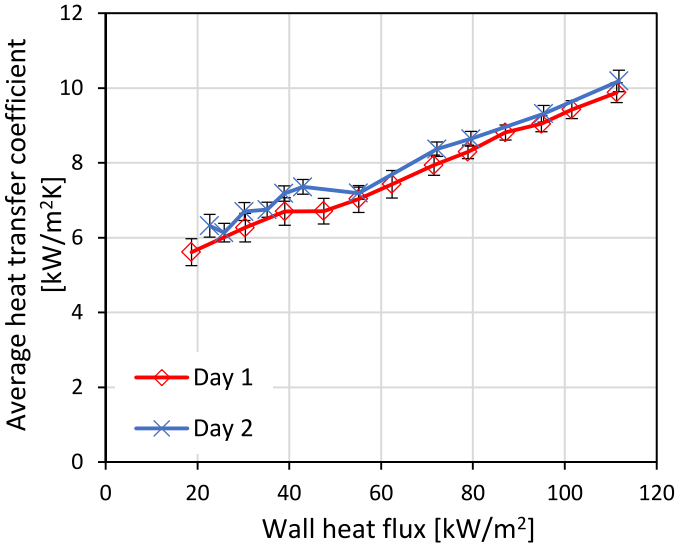

Fig. 8. Repeatability of the two-phase flow experiments at mass flux of 150 kg/m^{2}s for the aluminium heat sink.

5. Results and discussion

5.1. Flow patterns and flow reversal

The Phantom high-speed camera was used to capture the two-phase flow patterns at three locations along the centre of the heat sink, see Fig. 9-11. Generally, bubbly, slug, churn and annular flow were observed for the copper and aluminium heat sinks for the examined operating conditions with increasing heat flux. These flow patterns were also seen with decreasing heat flux. Fig. 9 was taken near the channel inlet at wall heat flux near 70 kW/m^2 and mass flux of 100 kg/m^{2}s. It can be seen that small bubbles, smaller than the channel width, were observed in both copper and aluminium heat sinks. Some of these bubbles originated at the channel corners. Confined bubbles were also captured in this figure, when the bubble size reached the channel width. The size and the distribution of these bubbles were similar for both microchannels, with some large bubbles present in both heat sinks. The captured images of the slug flow are shown in Fig. 10 at wall heat flux near 40 kW/m^2, mass flux of 150 kg/m^{2}s and near the channel middle. Vapour slugs with round ends filled these microchannels, with some bubbles in the trail of the vapour slugs. These features were found in both heat sinks and no clear difference can be seen. Fig. 11 depicts the annular flow at wall heat flux near 127 kW/m^2 and mass flux of 200 kg/m^{2}s at the channel outlet. The microchannels were filled by a continuous vapour core surrounded by a liquid film, the latter seen as a black layer at the channel side walls. No significant differences were observed between the

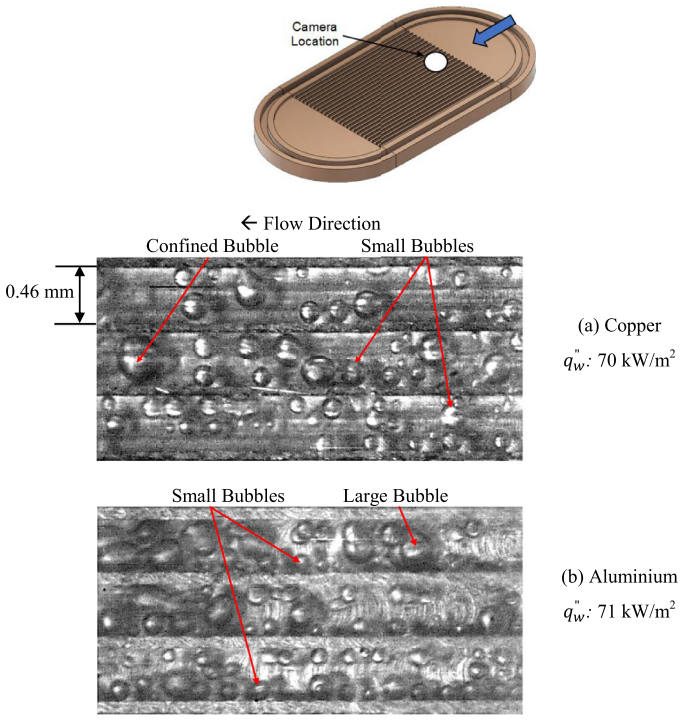

Fig. 9. Bubbly flow at wall heat flux near 70 kW/m^2 and mass flux of 100 kg/m^{2}s (near the channel inlet).

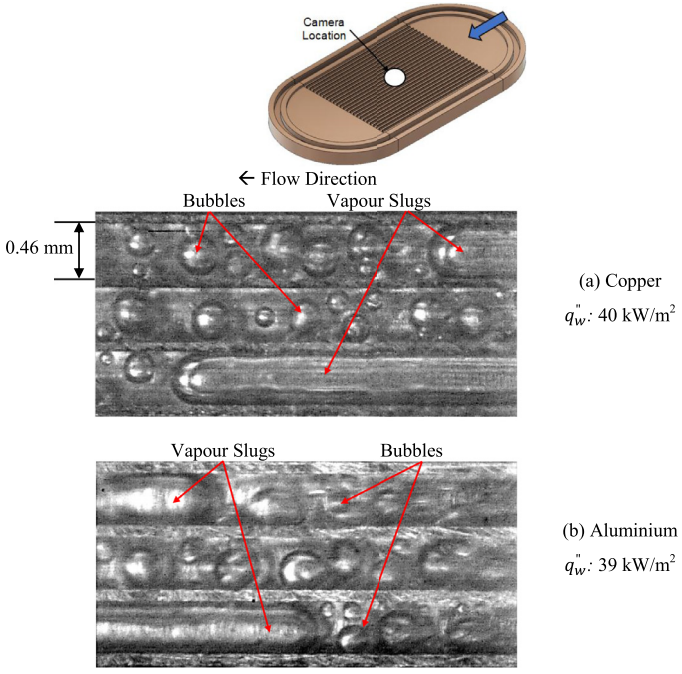

Fig. 10. Slug flow at wall heat flux near 40 kW/m^2 and mass flux of 150 kg/m^{2}s (near the channel middle).

two heat sinks examined. Note that, since the liquid film thickness around the channel circumference was very thin, it was difficult to measure it experimentally with the high-speed camera used in the present study. A conclusion reached here is that the flow patterns were not affected in any noitceable significant manner by the material of the heat sink, in this case copper and aluminium.

Flow reversal was observed in this study using both surfaces. During flow reversal, the flow patterns were fluctuating between bubbly, confined bubble and slug flow. In the present study, further image analysis was conducted to show the effect of this phenomenon on the bubble dynamics and liquid film features. Fig. 12 shows the bubble dynamics during flow reversal in copper heat sink at wall heat flux of 30.6 kW/m^2 and mass flux of 50 kg/m^{2}s. These sequencing pictures were captured near the channel inlet during 43 ms. The bubble diameter, the bubble departure diameter, the bubble growth time, the waiting time and the bubble generation frequency are discussed in this section. The Phantom camera control software was used to measure the bubble diameter by taking multiple measurements of a single bubble and calculating the average value. The bubble diameter is first measured after the bubble nucleates, while still at the nucleation site. The bubble departure diameter is measured when this bubble leaves this site. The bubble growth time is the time taken for the nucleated bubble to depart. The waiting time is the time between subsequent bubbles at the same nucleation site. The bubble generation frequency is calculated from the bubble growth time and the waiting time. At a designated time of 0 ms, a nucleating bubble was captured at the channel corner having a diameter of 118.7 μm (Bubble 1). This bubble departed the nucleation site at 3 ms, with a bubble departure diameter of 168 μm. As seen in this figure, this bubble slides on the wall side and moves towards the channel outlet with other bubbles. At 5 ms, a new bubble was seen at this site, having a diameter of 117.1 μm (Bubble 2). This bubble also departs the nucleation site and slides downstream at 8 ms with a departure diameter of 171.4 μm. The bubble growth time and the waiting time were 3 ms and 2 ms, respectively. It can be seen from these pictures that, when the flow moves towards the channel outlet, the average bubble departure diameter is 170 μm with a generation frequency of 200 Hz, i.e. 200 bubbles per second. This cycle was found to occur repeatedly from 8 to 14 ms. At 14 ms, a new bubble (Bubble 3) nucleated on the same site with the camera capturing this at a diameter of 114.8 μm. At 25 ms, this bubble was on the site and the bubble diameter increased to 165.9 μm. At this time flow reversal started to occur inside the channels. At 36 ms, the diameter of this bubble was 228.2 μm, with the bubble still on the

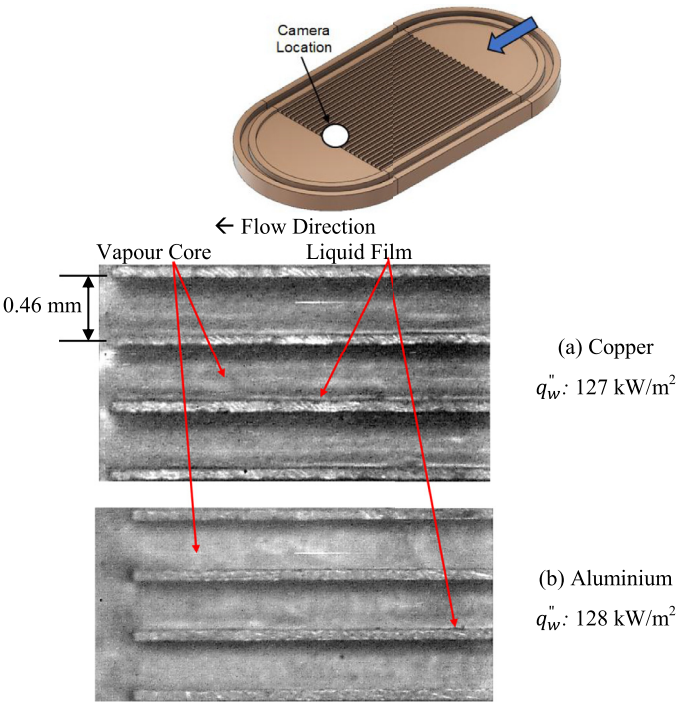

Fig. 11. Annular flow at wall heat flux near 127 kW/m^2 and mass flux of 200 kg/m^{2}s (at the channel outlet).

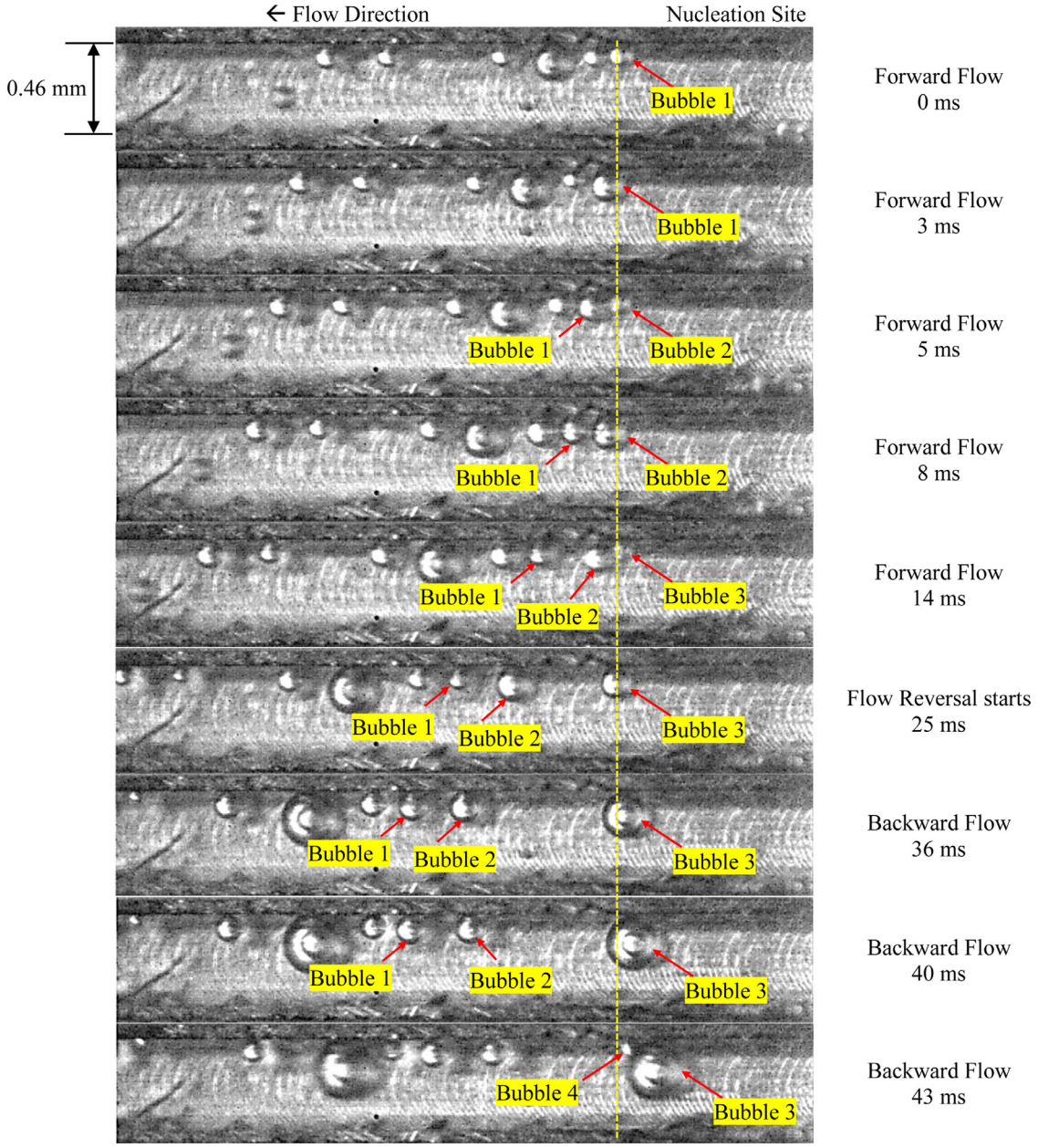

Fig. 12. Bubble dynamics during flow reversal in copper heat sink at wall heat flux of 30.6 kW/m^2 and mass flux of 50 kg/m^{2}s (near the channel inlet).

nucleation site. After 4 ms, the bubble was 267.6 μm in diameter and started to depart the site, but towards the channel inlet. At 43 ms, this captured bubble (Bubble 3) left the site towards the channel inlet with a diameter of 301.1 μm. As seen in the photograph a new bubble nucleated at this site (Bubble 4). The bubble generation frequency for these events was 26 Hz. It can be concluded that the bubble departure diameter increases due to longer time at the nucleation site during the flow reversal period and as consequence the bubble generation frequency decreases. The fact that the bubble size is larger in the period of flow reversal compared to the forward flow indicates a higher heat transfer component due to bubble generation to departure and local flow agitation, which in turn may abate the effects of flow reversal. In other words, flow reversal may have a small effect on the average two-phase heat transfer coefficient.

The features of liquid film in annular flow during flow reversal are shown in Fig. 13. The sequence of pictures in this figure was taken at wall heat flux of 117.8 kW/m^2 and mass flux of 200 kg/m^{2}s near the channel middle using the copper heat sink. Since the flow was annular, i.e. vapour core surrounding by liquid film, the flow direction during flow reversal was difficult to identify in these images. However, some distinctive flow features were captured by the camera. It can be seen from this figure that, at a designated time of 0 ms, the liquid film thickness was uniform and thin around the vapour core and along the channels. At 6 ms, fresh fluid was pushed into these channels, possibly due to the forward and backward motion caused by flow reversal. At 19 ms, the distribution of the liquid film was found not to be uniform, i.e. a wavy and thicker film. At 35 ms, the flow became more stable and the distribution of the liquid film was thinner and more uniform compared to that shown at 19 ms. Flow reversal could affect the distribution and the thickness of the liquid film, with a more intense reversal in the flow leading to non-uniform and thicker liquid film at the channel side walls.

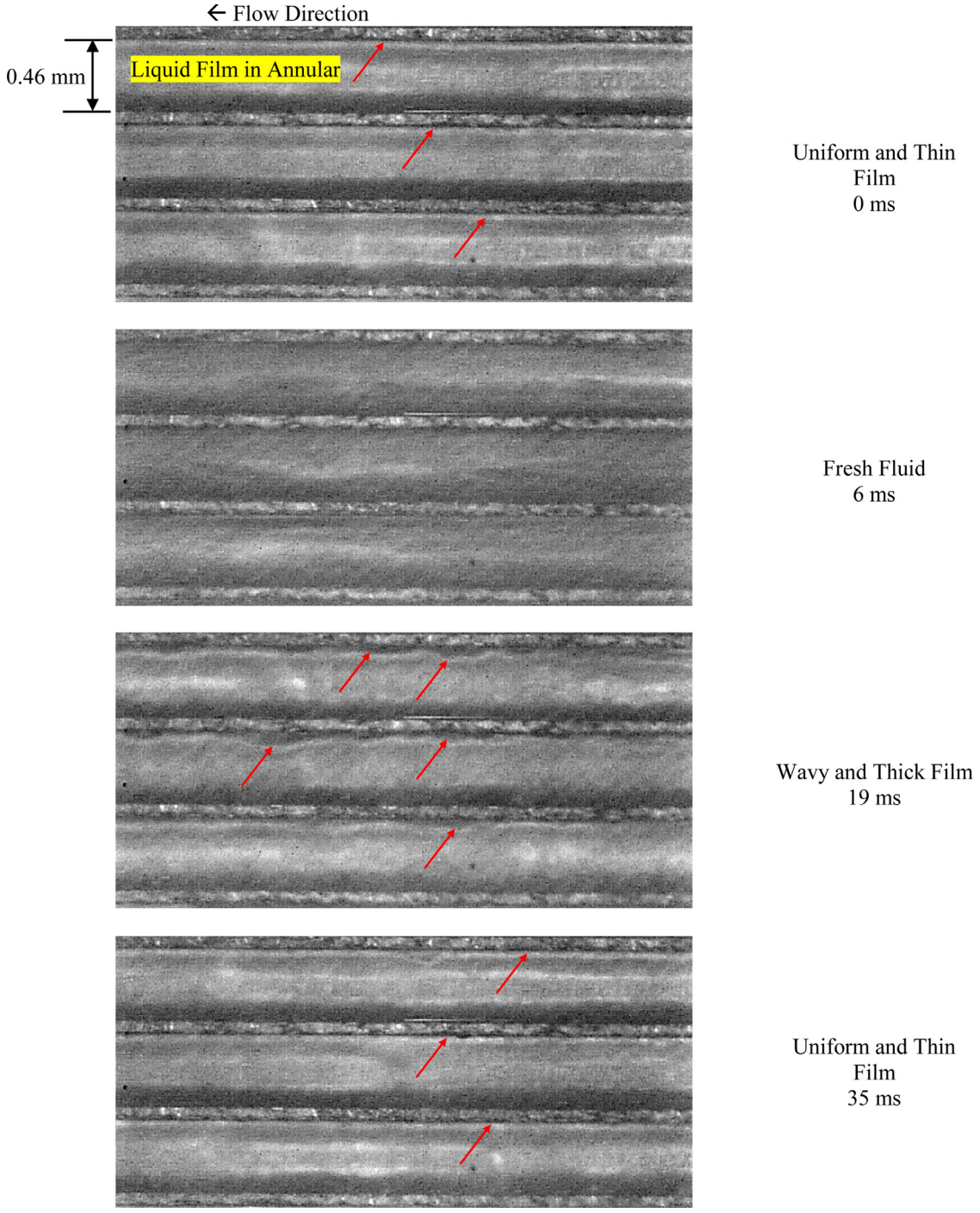

Fig. 13. Liquid film features during flow reversal in copper heat sink at wall heat flux of 117.8 kW/m^2 and mass flux of 200 kg/m^{2}s (at the channel middle).

The measured pressure drop fluctuation in both heat sinks is presented in Fig. 14 to clarify the flow reversal. This figure depicts the measured pressure drop fluctuation at a mass flux of 250 kg/m^{2}s and low and high wall heat fluxes. It can be seen that, for a given heat and mass flux, the aluminium heat sink provided higher measured pressure drop compared to copper. This is discussed further in Section 5.3. Lower pressure drop fluctuations were also seen in the aluminium heat sink. At low heat flux, 55 kW/m^2, the fluctuation amplitude of the measured pressure drop was found to be 0.16 (8% of the mean value) and 0.44 kPa (9% of the mean value) for aluminium and copper, respectively. This fluctuation increased to 0.56 kPa (8.5% of the mean value) and 2.37 kPa (47.4% of the mean value) for aluminium and copper surfaces, respectively, when the wall heat flux increased to 143 kW/m^2. The work by the present authors showed that flow reversal is, at least in part, due to the confined bubble expansion in both directions, i.e. when the slug flow starts to establish [16]. This higher pressure drop fluctuation in the copper heat sink could be due to the high bubble expansion rate (bubble interface velocity) compared to aluminium. Different surface topographies could be the reason for the different pressure drop fluctuation. As discussed in Section 2.2, the copper surface had fewer surface cavities compared to aluminium that may lead to lower number of nucleation sites resulting in higher wall temperature. High wall temperature could result in higher

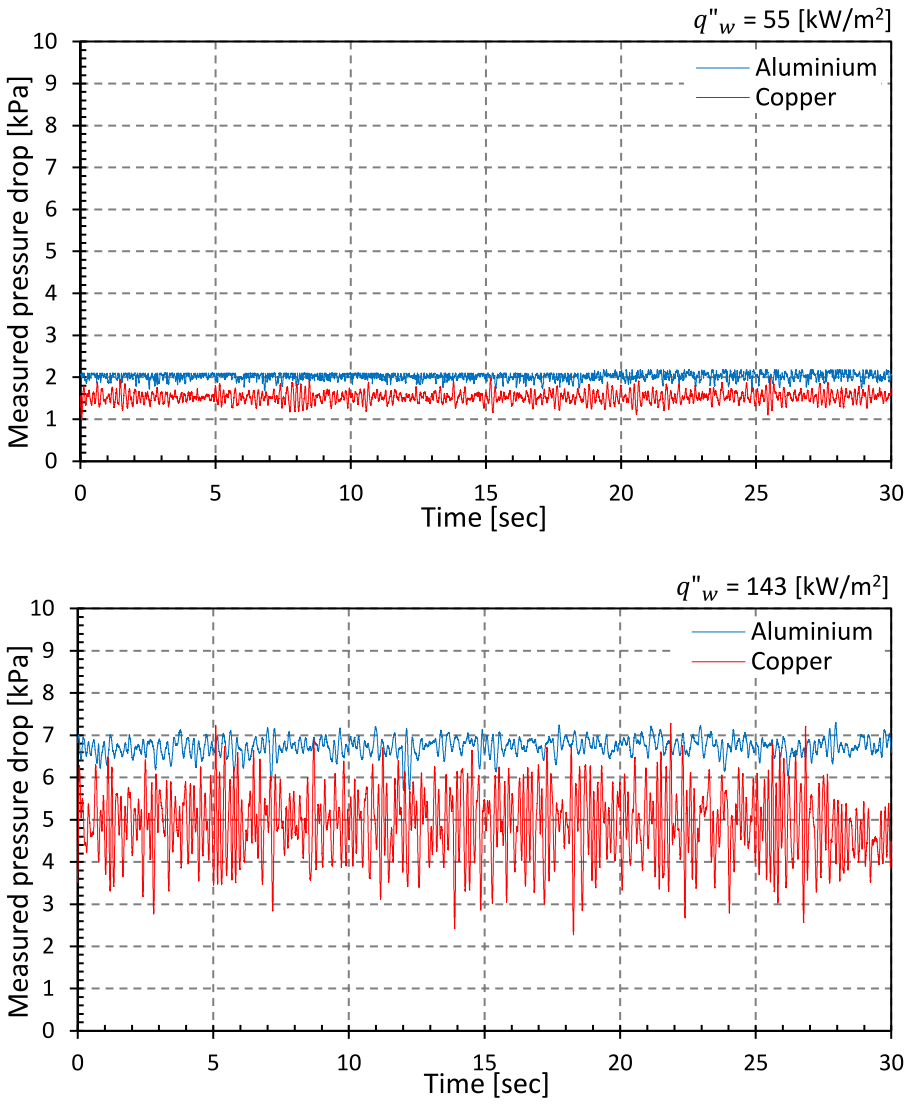

Fig. 14. Measured pressure drop fluctuation at mass flux of 250 kg/m^{2}s and two different wall heat fluxes.

evaporation rate and thus larger bubble expansion rate in both directions, when bubbles became confined by the channel sidewalls. This can lead to a higher possibility of reversal. Another reason for the increased bubble expansion and consequently pressure fluctuations in copper channels could be the large thermal diffusivity of copper compared to aluminium (1.5 times larger), i.e. heat can be conducted at a faster rate to the bubbles.

5.2. Two-phase heat transfer coefficient

The two-phase heat transfer coefficient and vapour quality were calculated locally at three locations along the channels, see Eq. (14) and (23), respectively, in Section 3. These parameters were then plotted for both heat sinks at low and high wall heat fluxes as shown in Fig. 15. This figure indicates that, at boiling incipience, the local two-phase heat transfer coefficient reached a maximum value then decreased with further increase in the local vapour quality. This decrease could be due to the flow patterns changes, i.e. from bubbly to slug, churn and later annular flow. The heat transfer rate may be higher in the nucleate boiling region and lower during the other flow patterns, see [29,30]. Steinke and Kandlikar [31] also mentioned that a high heat transfer coefficient was found at low quality due to the onset of nucleate boiling. After that, the heat transfer coefficient decreased with quality due to the rapid bubble growth leading to slug and annular flow and then flow reversal and dry-out.

Fig. 15(a) shows that, at low wall heat flux of 31 kW/m^2, there was an insignificant difference in the local heat transfer coefficient for both heat sinks. This changed when the heat flux was increased (higher wall superheat) as shown in Fig. 15(b). This is probably due to the fact that as the temperature difference increases, cavities with a wider range of radii become active, see [32] and these are more plentiful on the aluminium surface. These larger numbers of active nucleation sites explains the higher heat transfer rates in the aluminium heat sink. The above discussion is also relevant to Fig. 16, which depicts the average two-phase heat transfer coefficient, given by equation 25, at a mass flux of 250 kg/m^{2}s using both heat sinks. As seen in the figure, the heat transfer coefficient increased with wall heat flux for both heat sinks indicating the increased contribution of nucleate boiling. The figure also indicates that there was an insignificant difference between these sinks at wall heat flux less than 80 kW/m^2. Beyond that, the larger number of possible active nucleation sites affects the heat transfer rates with aluminium giving higher rates as discussed above. At the highest value of heat flux at this mass flux, the average two-phase heat transfer coefficient in aluminium was 20% higher

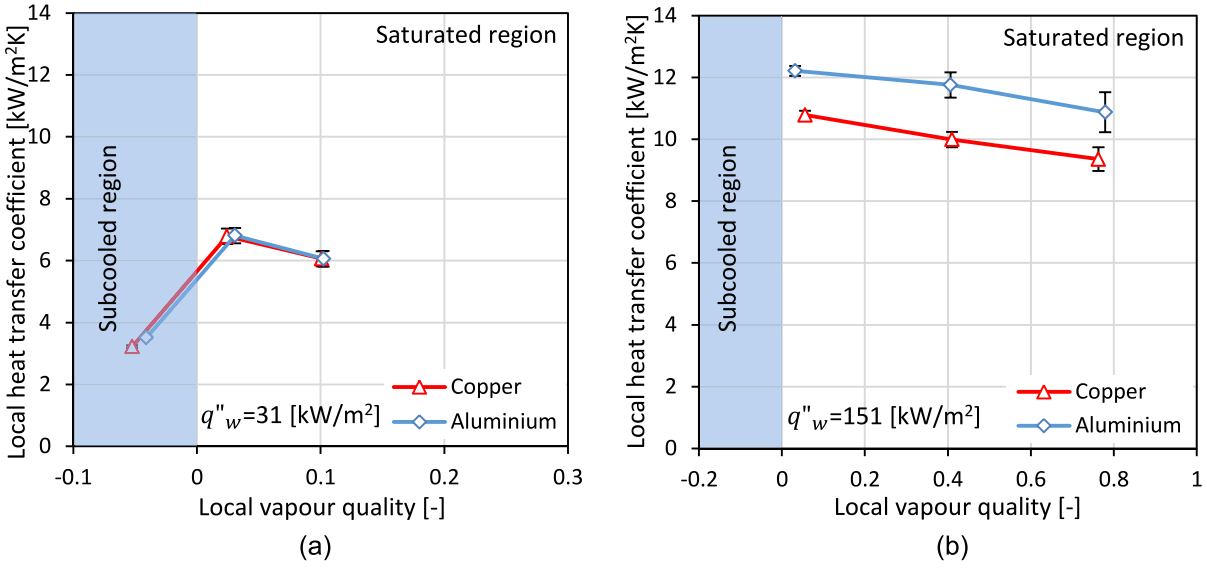

Fig. 15. Local heat transfer coefficient at mass flux of 250 kg/m^{2}s for (a) Low wall heat flux (b) High wall heat flux.

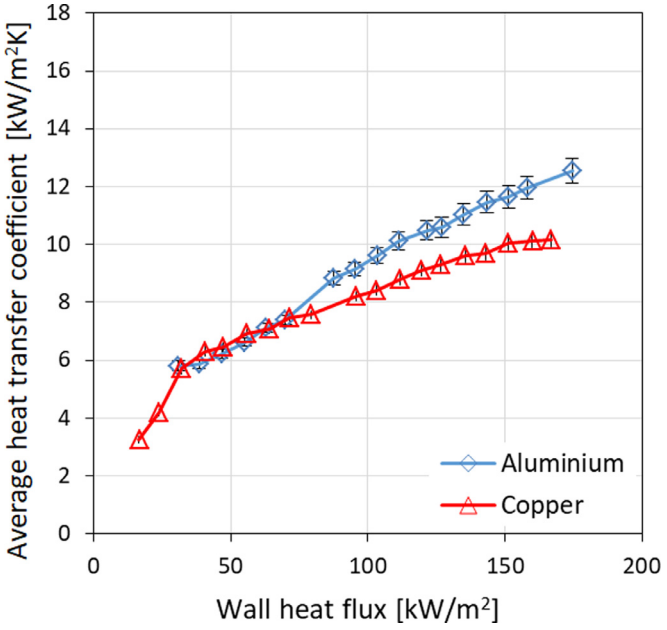

Fig. 16. Average two-phase heat transfer coefficient at mass flux of 250 kg/m^{2}s.

compared to copper. Over this range of heat fluxes, the aluminium heat sink provided a 12% higher average two-phase heat transfer coefficient compared to copper.

Different materials may have significantly different thermal conductivity and surface roughness/microstructure and wettability with certain fluids. The thermal conductivity of copper is approximately twice that of aluminium. The present results showed that there is a noticeable enhancement, but by 12% on average, when using the aluminium heat sink and hence this conductivity difference cannot account for the different heat transfer coefficient. The surface roughness measurements indicated that copper has higher average surface roughness compared to aluminium. Rougher surface channels are expected to show higher heat transfer coefficient, which is contrary to the present experimental results. HFE-7100 has very low surface tension (0.0136 N/m at 1 bar) and is considered a super-hydrophilic refrigerant. The contact angle of this refrigerant is nearly zero on all surface types as reported by [33]. It is worth mentioning that the static contact angle of HFE-7100 was measured on the copper and aluminium surfaces in this study using the sessile drop standard method and the droplet spread completely on both surfaces. Accordingly, wettability is not expected to be the reason for the different heat transfer rates seen in the copper and aluminium heat sinks. Therefore, this leads to the conclusion that the different heat transfer coefficient results could be due to the different surface microstructures (cavity number, shape and size), which affects the active nucleation site density and subsequent the establishment of flow patterns and their proportional length along the flow direction and probably the liquid film thickness. It was not possible to measure the nucleation site density in our experiments, especially with increasing heat flux. Therefore, the correlation of Benjamin and Balakrishnan [34] for pool boiling was adopted here, see Eq. (41), in order to calculate the number of active nucleation sites on both surfaces.

$$NSD = 218.8 Pr_l^{1.63} \left(\frac{1}{\gamma}\right) \theta^{-0.4} (\Delta T_{sup})^3 \tag{41}$$

$$\gamma = \left(\frac{k_w \rho_w c_{pw}}{k_l \rho_l c_{pl}}\right)^{0.5} \tag{42}$$

$$\theta = 14.5 - 4.5\left(\frac{RaP}{\sigma}\right) + 0.4\left(\frac{RaP}{\sigma}\right)^2 \tag{43}$$

This pool boiling empirical correlation was proposed and verified by [34] using different fluids and materials, such as stainless steel, nickel, aluminium and copper. It covered several parameters, namely the wall superheat, the thermophysical properties of fluid and heating surface, the heating surface roughness and the fluid surface tension. The thermophysical propoerties of fluid were found at the inlet pressure, while the wall temperature was used to find the solid properties. Fig. 17 presents the nucleation site density versus wall superheat for both surfaces at a mass flux of 250 kg/m^{2}s. This figure was plotted for a wall superheat at an axial distance (z/L) of 0.1, where bubbly flow occurrs. As seen in the figure, the active nucleastion sites increased with increasing wall superheat for both materials, with the aluminium surface having a higher possible nucleation site density than copper for a given wall superheat. Figure 17 demonstrates also that for a fixed superheat of 12 K, as an example, the NSD in aluminium is about 50% larger than that in copper. Thus, it was expected that the enhancement in heat transfer coefficient in the aluminium heat sink should

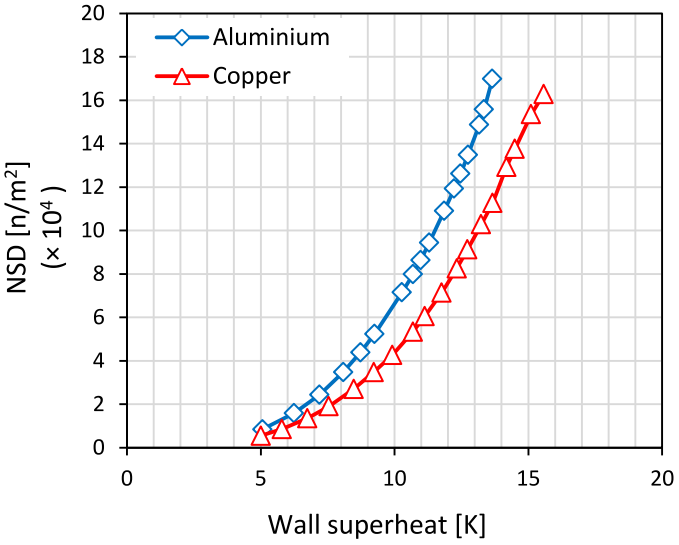

Fig. 17. Nucleation site density at mass flux of 250 kg/m^{2}s and z/L of 0.1.

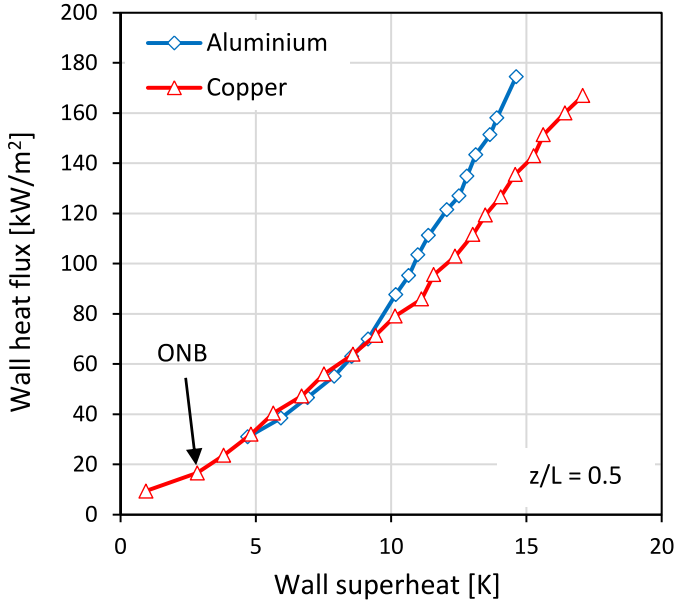

Fig. 18. Boiling curve at mass flux of 250 kg/m^{2}s and z/L of 0.5.

be about 50% or larger. However, the obtained average enhancemnet in the present study was 12%. The reason could be due to the fact that Eq. (41) was proposed for pool boiling while in flow boiling, due to the flow velocity, the thermal boundary layer thickness is much smaller and thus some of the nucleation sites can be supressed.

The boiling curve of HFE-7100 at mass flux G = 250 kg/m^2 s is presented in Fig. 18. The wall heat flux is plotted against the wall superheat. This figure illustrates that the boiling incipience (Onset of Nucleate Boiling-ONB) occurred at wall heat flux near 20 kW/m^2 and can be seen at this heat flux without temperature overshoot. This ONB was obtained from the flow visualization results. The absence of temperature overshoot could be due to the rough channel surfaces, i.e. Ra = 0.286 and 0.192 μm for copper and aluminium channels, respectively, which allows nucleate boiling to commence without a significant temperature overshoot, see [32]. After the ONB, the wall heat flux increased smoothly with the wall superheat. The experiments were run until an exit vapour quality of one was reached at 174 kW/m^2 at a mass flux of 250 kg/m^{2}s. It can be

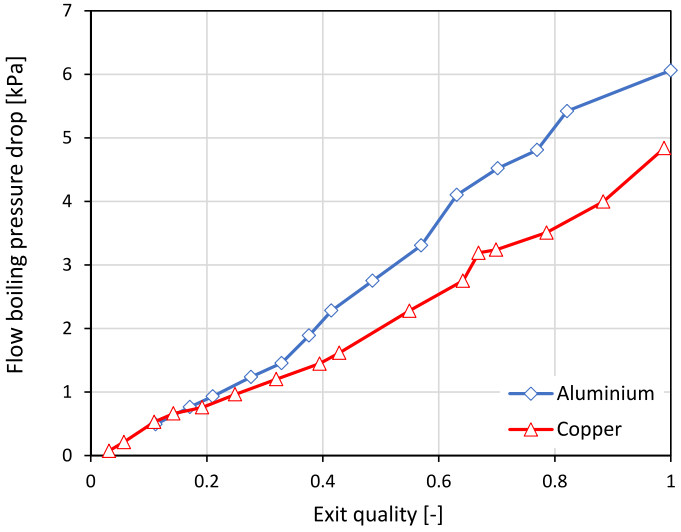

Fig. 19. Two-phase pressure drop at mass flux of 200 kg/m^{2}s.

seen from this figure that there was no difference between the two heat sinks up to a degree of superheat of 10 K, which corresponds to a wall heat flux of 80 kW/m^2. However, as mentioned above, at wall heat fluxes more than this value, the aluminium heat sink provided higher wall heat flux by approximately 29 % at the highest heat flux and, as mentioned above, with average difference of 12 % compared to copper for the range of heat flux studied.

5.3. Two-phase pressure drop

The two-phase pressure drop versus exit vapour quality at a mass flux of 200 kg/m^{2}s, obtained using Eq. (16), is presented in Fig. 19. The two-phase pressure drop increased with exit quality (heat flux) for both heat sinks due to the increasing bubble generation and flow resistance. This figure also shows that the aluminium heat sink had higher flow boiling pressure drop than that of copper, when the exit vapour quality was more than 0.2, i.e. wall heat flux of 55 kW/m^2. At the highest examined mass flux of 250 kg/m^{2}s, the maximum flow boiling pressure drop of 5.5 and 7.8 kPa was found with the copper and aluminium heat sinks, respectively. At this mass flux, the flow boiling pressure drop increased by 28 % (average difference) with the aluminium heat sink.

Both acceleration and frictional pressure drop components are presented in Fig. 20 at a mass flux of 200 kg/m^{2}s in order to clarify this difference in the pressure drop results. The acceleration component was calculated using the void fraction given in [23], see Eq. (38-39) in Section 3. The frictional component was found by subtracting the acceleration component from the two-phase pressure drop, see Eq. (40). Fig. 20(a) indicates that there was no difference in the acceleration pressure drop component. For given heat and mass flux values, the exit vapour quality was nearly the same for both heat sinks. As a result, the void fraction and thus the acceleration pressure drop component showed an insignificant difference. In contrast, the trend of the frictional pressure drop component was completely different as shown in Fig. 20(b). It depicts that the aluminium heat sink had a higher frictional pressure drop component than copper. This became significant at vapour qualities more than 0.2 (wall heat flux of 55 kW/m^2). Pike-Wilson [35] studied flow boiling of R245fa in vertical metallic tubes having 1.1 mm inner diameter and made of copper, brass and stainless steel and demonstrated that both number and shape of surface peaks (surface microstructures) could restrict the flow and affect the frictional pressure drop. Similarly, the frictional pressure drop in the present study, is higher in the aluminium heat sink due to the dif-

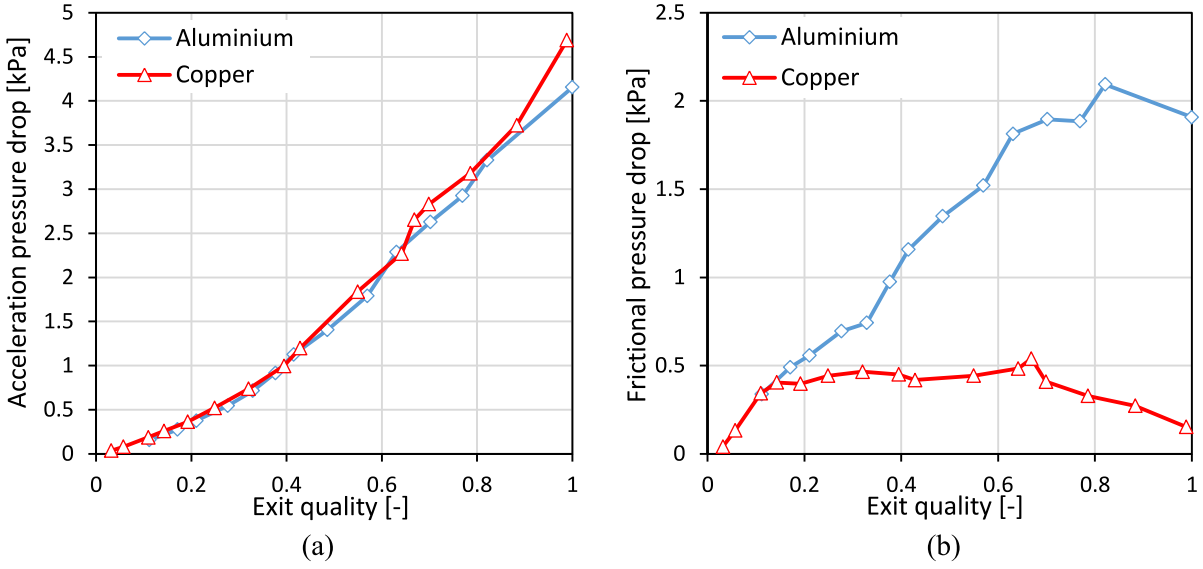

Fig. 20. Two-phase pressure drop components at mass flux of 200 kg/m^{2}s on: (a) Acceleration component (b) Frictional component.

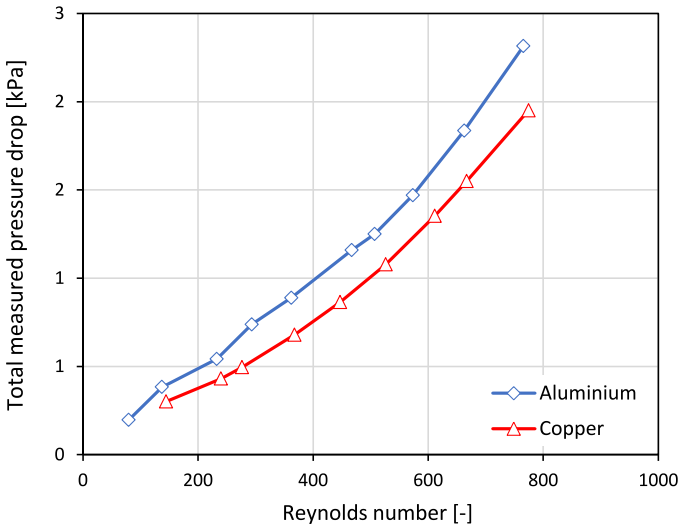

Fig. 21. Single-phase total pressure drop versus Reynolds number.

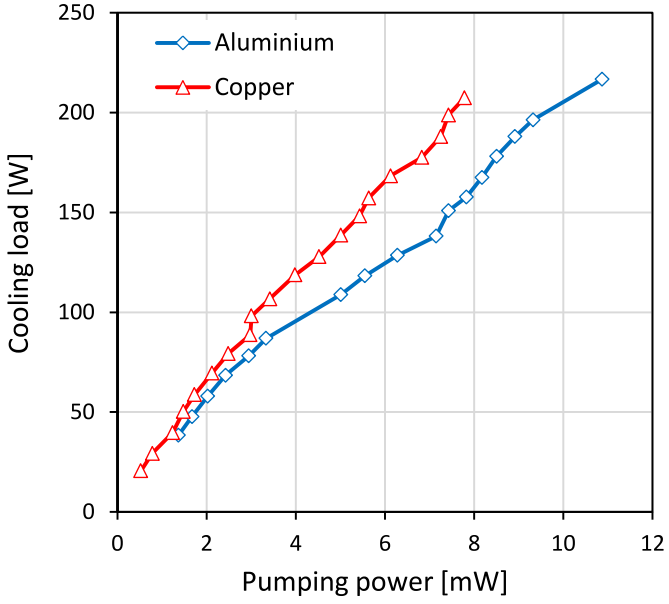

Fig. 22. Cooling load versus pumping power at mass flux of 250 kg/m^{2}s.

ferent surface microstructures. In order to assess the effect of frictional pressure drop, the single-phase total pressure drop (ΔP_{meas}) versus Reynolds number is presented in Fig. 21. As seen in the figure, the measured pressure drop increased with Reynolds number due to an increase in the mass flow rate. It is higher in the aluminium heat sink, explaining also the higher frictional pressure drop during two-phase flow and the higher total pressure drop in this heat sink.

5.4. Thermal performance of different heat sink metals

The thermo-fluid performance of the two heat sinks is depicted Fig. 22 and 23. The pumping power was calculated using Eq. (37) based on the total measured pressure drop across the heat sink including the single-phase region, the two-phase region, and the inlet and outlet plena. Fig. 22 depicts the cooling load variation with increasing pumping power in both heat sinks. The figure shows that, for a given pumping power, both metals provided similar cooling loads (q''_b times 20 mm x 25 mm) at cooling load less than 90 W, which corresponds to a wall heat flux of 72.5 kW/m^2. However, at cooling load higher than 90 W, the copper heat sink achieved higher cooling loads for a given pumping power required than those in the aluminium heat sink. This is due to the higher two-phase pressure drop in the aluminium heat sink at the same cooling load (heat flux), as discussed in Section 5.3. The maximum cooling load achieved in our study was 217 W (base heat flux of 434 kW/m^2). And at this load the pumping power required by the aluminium heat sink was 37% higher than that required by the copper heat sink. It is worth noting however that the maximum power consumption by the pump to circulate the flow in the heat sink (including losses in the two plena) was 11 mW at the maximum cooling load of 217 W using aluminium heat sink, which is still small power consumption.

Fig. 23 depicts the total thermal resistance versus the cooling load using both metals at mass flux of 250 kg/m^{2}s calculated using Eq. (31) and the simplified form in Eq. (32). This mass flux was chosen since it provided higher cooling load. Fig. 23(a) demon-

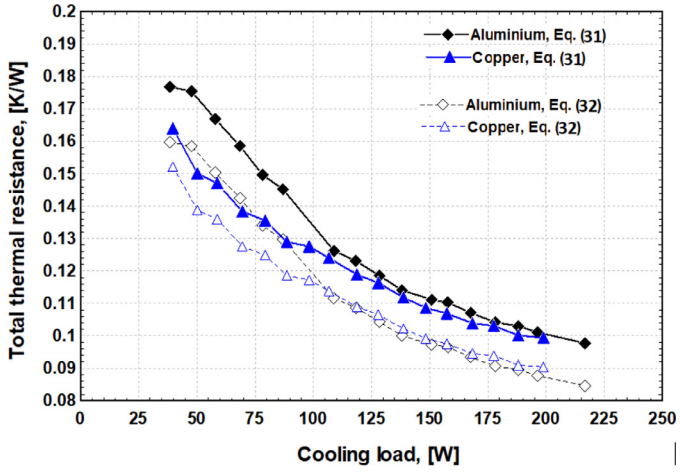

(a)

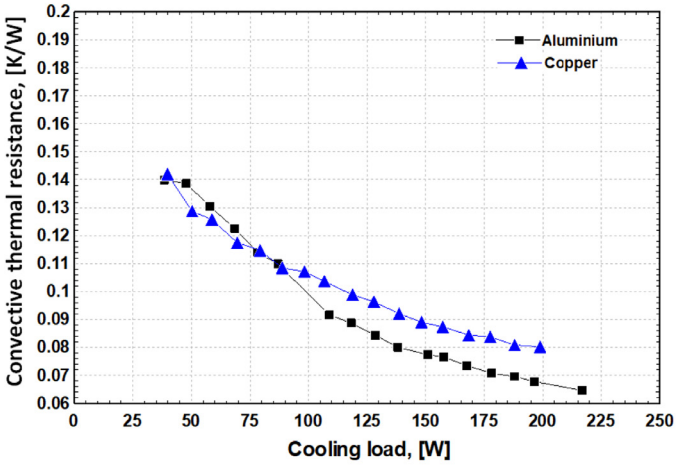

(b)

Fig. 23. Thermal resistance versus cooling load at mass flux of 250 kg/m^{2}s. (a) Total thermal resistance (b) Flow boiling convective thermal resistance.

strates that the total thermal resistance decreased with increasing cooling load. This is due to the increasing heat transfer coefficient in the channels as the heat flux (cooling load) increases, see Fig. 16. At low cooling load values (less than 90 W) the total thermal resistance of aluminium heat sink was 7–13 % higher than that of copper. This is due to the higher conductive resistance by this metal (0.019 K/W) compared to copper (0.01 K/W). For cooling loads above 90 W, the difference in total thermal resistance for the two heat sinks is insignificant. It is worth noting that ignoring the conduction resistance in the fins (Eq. (32)) resulted in slightly lower resistances compared to using all resistances in Eq. (31). For aluminium and copper, the resistance was lower by 9.6–13.5% and 7.3–9.1%, respectively. Moreover, there was no significant difference in the convective thermal resistance for both metals as shown in Fig. 23(b) especially for cooling loads below 90 W while copper exhibited about 16 % larger convective resistance for loads above 90 W. This is due to the fact that the heat transfer results were not significantly different at wall heat flux less than 72.5 kW/m^2, i.e. cooling load of 90 W, as discussed in Section 5.2. Although the aluminium surface had higher conductive thermal resistance, it also provided lower convective thermal resistance at these cooling loads as seen in Fig. 23(b). It is worth mentioning that the maximum wall temperature for the two metals was 80°C. The temperature above is within the allowable operational temperature for electronic chips thus making both aluminium and copper suitable choices for such applications. Further, one must note that the thermal performance of any heat sink could change during a long-running period. This issue may become more noticeable when using flow boiling in micro-scale configurations with refrigerants having high concentration of air. For example, at standard pressure and temperature, a unit of refrigerant HFE-7100 liquid contains 0.53 units of air by volume, i.e. 366 ppm concentration [36]. This value is much higher than other fluids. For example, the concentration of air in water is just 8.5 ppm at the same conditions, see [36]. High concentration of air may cause surface aging leading to a reduction in the heat transfer performance as discussed by [19]. This may affect the heat transfer rates and should be considered further to clarify the extend of this change.

6. Conclusions

This study presented the thermal performance of microchannel heat sinks using two different metals and HFE-7100 as the test fluid. Two heat sinks made of copper and aluminium with channel hydraulic diameter of 0.46 mm were tested experimentally. The flow boiling performance was assessed at 1 bar system pressure, 5 K inlet sub-cooling, 50–250 kg/m^{2}s mass flux and wall heat flux up to 174 kW/m^2. The main conclusions from this study are given below.

Bubbly, slug, churn and annular flow were visualised for both heat sinks when the heat flux was changed gradually. Different metals did not show a significant difference in the captured flow patterns.

The copper microchannel heat sink exhibited higher levels of flow reversal than the aluminium one. This was indicated by the measured pressure drop fluctuation, being higher in the copper evaporator. The visualization of flow reversal showed that the bubble departure diameter increased, while the bubble generation frequency decreased. Moreover, the liquid film became non-uniform and thicker during this phenomenon.

The heat transfer results indicated that the local two-phase heat transfer coefficient was high at very low local vapour quality and then decreased with increasing qualities. The heat transfer coefficient increased with increasing wall heat flux. Both local and average two-phase heat transfer coefficients were higher for the aluminium heat sink compared to the copper one. This was found at moderate and high wall heat fluxes, while insignificant effect was found at low ranges. This trend, as the heat flux increased, was due to the possible activation of the higher number of cavities found on the aluminium surface.

The two-phase pressure drop increased with exit vapour quality (heat flux). The aluminium heat sink had a higher pressure drop than copper. This became obvious with increasing vapour quality and was the result of a higher frictional component in the aluminium heat sink due to the different surface characteristics of the two metallic surfaces.

The thermal performance of these heat sinks indicated that, for a given cooling load, aluminium heat sink had higher pumping power. However, this pumping power was very small (11 mW) so this is not a factor in determining what metal to use in the microchannels heat sinks. This metal also showed that the total thermal resistance was higher compared to copper. However, this value decreased with further increase in the cooling load and became close to the copper resistance.

The present study indicates that multi-microchannel heat sinks made of aluminium could be a suitable choice for use as microchannel evaporators for cooling high heat flux devices. In comparison with the copper evaporator, the aluminium microchannels are characterised by light weight, low cost, high corrosion resis-

tance and lower flow instability. And since their overall fluid flow and heat transfer performance is comparable to the copper heat sinks it can also be considered as one of the choices for microchannel heat exchangers in flow boiling applications.

The base heat flux achieved in the present experiments was up to 434 kW/m^2, corresponding to the cooling load of 217 W for a high heat flux device of 500 mm^2, and maximum wall temperature of 80°C. Higher base loads are possible for higher mass flow rates and higher operating pressures.

Author Statement

T.G. Karayiannis: Conceptualisation, methodology, analysis and interpretation of results, editing, reviewing.

A. Al-Zaidi: Experiments, analysis and interpretation of results, writing.

M.M. Mahmoud: Analysis and interpretation of results, editing, reviewing

Declaration of Competing Interest

The authors declare the following financial interests/personal relationships which may be considered as potential competing interests:

T.G. Karayiannis reports financial support was provided by Engineering and Physical Sciences Research Council.

Acknowledgements

Ali Al-Zaidi would like to thank the Iraqi Ministry of Higher Education and Scientific Research (MOHESR) for their financial support during his PhD studies at Brunel University London. The support of EPSRC through grant EP/K01112/1 and the current grant of EP/T033045/1 is acknowledged.

References

[1] T.G. Karayiannis, M.M. Mahmoud, Flow boiling in microchannels: Fundamentals and applications, Appl. Therm. Eng. 115 (2017) 1372–1397.
[2] K. Gottschalk, "IBM HPC Technology & Strategy," in *Hyperion HPC User Forum Stuttgart*, 2018, pp. 1–19.
[3] K.H. Bang, W.H. Choo, Flow boiling in minichannels of copper, brass, and aluminum round tubes, in: Proceedings of ICMM2004, the 2nd International Conference on Microchannels and Minichannels, 2004, pp. 1–6.
[4] E.A. Pike-Wilson, T.G. Karayiannis, Flow boiling of R245fa in 1.1mm diameter stainless steel, brass and copper tubes, Exp. Therm. Fluid Sci. 59 (2014) 166–183.
[5] C.L. Vandervort, A.E. Bergles, M.K. Jensen, An experimental study of critical heat flux in very high heat flux subcooled boiling, Int. J. Heat Mass Transf. 37 (1994) 161–173.
[6] B.J. Jones, S.V. Garimella, Surface Roughness Effects on Flow Boiling in Microchannels, J. Therm. Sci. Eng. Appl. 1 (4) (2009).
[7] T. Alam, P.S. Lee, C.R. Yap, Effects of surface roughness on flow boiling in silicon microgap heat sinks, Int. J. Heat Mass Transf. 64 (2013) 28–41.
[8] R. Jafari, T. Okutucu-Özyurt, H.Ö. Ünver, Ö. Bayer, Experimental investigation of surface roughness effects on the flow boiling of R134a in microchannels, Exp. Therm. Fluid Sci. 79 (2016) 222–230.
[9] V. Rodriguez, J. Sukumaran, M. Ando, and P. De Baets, "Roughness Measurement Problems in Tribological Testing," in *Sustainable Construction and Design (SCAD)*, 2011, pp. 115–121.
[10] T.G. Karayiannis, M.M. Mahmoud, D.B.R. Kenning, A study of discrepancies in flow boiling results in small to microdiameter metallic tubes, Exp. Therm. Fluid Sci. 36 (2012) 126–142.
[11] K. Vontas, M. Andredaki, A. Georgoulas, N. Miché, M. Marengo, The effect of surface wettability on flow boiling characteristics within microchannels, Int. J. Heat Mass Transf. (2021) 121133.
[12] R. Ahmadi, T. Okawa, Influence of surface wettability on bubble behavior and void evolution in subcooled flow boiling, Int. J. Therm. Sci. 97 (2015) 114–125.
[13] C. Choi, J.S. Shin, D.I. Yu, M.H. Kim, Flow boiling behaviors in hydrophilic and hydrophobic microchannels, Exp. Therm. Fluid Sci. 35 (5) (2011) 816–824.
[14] K. Tan, Y. Hu, Y. He, Effect of wettability on flow boiling heat transfer in a microtube, Case Stud. Therm. Eng. 26 (2021).
[15] H. Trieu, N. Caney, P. Marty, S. Colasson, J. Gavillet, Flow boiling of water in a minichannel : The effects of surface wettability on two-phase pressure drop, Appl. Therm. Eng. 31 (2011) 1894–1905.
[16] A.H. Al-Zaidi, M.M. Mahmoud, T.G. Karayiannis, Flow boiling of HFE-7100 in microchannels: Experimental study and comparison with correlations, Int. J. Heat Mass Transf. 140 (2019) 100–128.
[17] A.H. Al-Zaidi, M.M. Mahmoud, T.G. Karayiannis, Effect of aspect ratio on flow boiling characteristics in microchannels, Int. J. Heat Mass Transf. 164 (2021) 120587.
[18] Clinton Aluminum, "Best aluminum alloys for heat transfer," *April 27*, 2017. https://www.clintonaluminum.com/best-aluminum-alloys-for-heat-transfer/ (accessed May 25, 2018).
[19] P. Jayaramu, S. Gedupudi, S.K. Das, An Experimental Investigation on the Influence of Copper Ageing on Flow Boiling in a Copper Microchannel, Heat Transf. Eng. 41 (4) (2020) 333–350.
[20] R. Remsburg, *Thermal design of electronic equipment*. 2001.
[21] J.G. Collier, J.R. Thome, *Convective Boiling and Condensation*, Third edit, Oxford University Press, Oxford, UK, 1994.
[22] R.K. Shah, A.L. London, Laminar flow forced convection in ducts, Supplement 1 to Advances in Heat Transfer, Academic Press, New York, 1978.
[23] S.M. Zivi, Estimation of steady-state steamvoid-fraction by means of the principle of minimum entropy production, J. Heat Transf. 86 (1964) 247–252.
[24] H.W. Coleman, W.G. Steele, Experimentation and uncertainty analysis for engineers, 3nd ed., Wiley, Chichester, New York, 2009.
[25] A.H. Al-Zaidi, M.M. Mahmoud, T.G. Karayiannis, Condensation Flow Patterns and Heat Transfer in Horizontal Microchannels, Exp. Therm. Fluid Sci. 90 (2018) 153–173.
[26] K. Stephan, P. Preuber, Warmeubergang und Maximale Warmestromdichte Beim Behaltersieden Binarer und Ternarer Flussigkeitsgemische, Chem. Ing. Tech. 51 (1979) 37.
[27] X.F. Peng, G.P. Peterson, Convective heat transfer and flow friction for water flow in microchannel structures, Int. J. Heat Mass Transf. 39 (12) (1996) 2599–2608.
[28] M. Mirmanto, Single-phase flow and flow boiling of water in horizontal rectangular microchannels, Brunel University London, London, UK, 2013 (PhD thesis).
[29] V.Y.S. Lee, G. Henderson, Al. Reip, T.G. Karayiannis, Flow Boiling Heat Transfer in Plain and Porous Coated Microchannel Heat Sinks, Int. Journal of Heat and Mass Transfer 183 (2022).
[30] V.Y.S. Lee, T.G. Karayiannis, Effect of Inlet Subcooling on Flow Boiling in Microchannels, Appl. Therm. Eng. 181 (2020) 115966.
[31] M.E. Steinke, S.G. Kandlikar, An Experimental Investigation of Flow Boiling Characteristics of Water in Parallel Microchannels, J. Heat Transfer 126 (4) (2004) 518–526.
[32] M. M. Mahmoud and T. G. Karayiannis, "Pool Boiling Review: Part I - Fundamentals of Boiling and Relation to Surface Design," *Therm. Sci. Eng. Prog.*, pp. 1–33.
[33] W. Li, J. Ma, T. Alam, F. Yang, J. Khan, C. Li, Flow boiling of HFE-7100 in silicon microchannels integrated with multiple micro-nozzles and reentry micro-cavities, Int. J. Heat Mass Transf. 123 (2018) 354–366.
[34] R.J. Benjamin, A.R. Balakrishnan, Nucleation Site Density in Pool Boiling of Saturated Pure Liquids: Effect of Surface Microroughness and Surface and Liquid Physical Properties, Exp. Therm. Fluid Sci. 15 (1) (1997) 32–42.
[35] E.A. Pike-Wilson, Flow boiling of R245fa in vertical small metallic tubes, Brunel University London, London, UK, 2014 (PhD thesis).
[36] L.C. Hsu, S.W. Cion, K.W. Lin, C.C. Wang, An experimental study of inclination on the boiling heat transfer characteristics of a micro-channel heat sink using HFE-7100, Int. Commun. Heat Mass Transf. 62 (2015) 13–17.